

Precise determination of the three-quark potential in SU(3) lattice gauge theory

Yoshiaki Koma*

National Institute of Technology, Numazu College, Ooka 3600, Numazu 410-8501, Japan

Miho Koma†

Nihon University, College of International Relations, Mishima 411-8555, Japan

(Received 20 March 2017; published 31 May 2017)

We investigate the static interquark potential for the three-quark system in SU(3) lattice gauge theory at zero temperature by using Monte Carlo simulations. We extract the potential from the correlation function of the three Polyakov loops, which are computed by employing the multilevel algorithm. We obtain remarkably clean results of the three-quark potential for $O(200)$ sets of the three-quark geometries including not only the cases that three quarks are put at the vertices of acute, right, and obtuse triangles, but also the extreme cases such that three quarks are put in line. We find several new interesting features of the three-quark potential and then discuss its possible functional form.

DOI: [10.1103/PhysRevD.95.094513](https://doi.org/10.1103/PhysRevD.95.094513)

I. INTRODUCTION

The static interquark potential for a three-quark system, the three-quark potential, is one of the characteristic quantities in quantum chromodynamics (QCD), which is relevant to spectroscopy of hadrons, especially, of baryons. Therefore it is quite important to determine the functional form of the potential from the first principle, clarify the properties of the three-quark system. Since a direct interaction among three quarks, a three-body force, is expected in QCD by virtue of SU(3) gauge symmetry, it is also interesting to investigate how the three-quark potential is different from or the same as the two-body quark-antiquark potential.

The investigation of the static interquark potential generally requires a nonperturbative method as the quarks are strongly interacting with each other inside hadrons, and Monte Carlo simulations of lattice QCD offer a powerful tool for this purpose. The first lattice study of the three-quark potential goes back to the mid-1980s by Sommer and Wosiek [1,2], and by Thacker *et al.* [3]. The study was revisited around 2000 by several groups with improved numerical techniques and computer resources [4–7].

These latest results were, however, found to be inconsistent with each other. Bali [4] and Alexandrou *et al.* [7] claimed that the potential was described by the half of the sum of two-body potentials in the quark-antiquark system, which is called the Δ area law, up to the interquark distance nearly 1 fm.¹ At the distances where the perturbation theory cannot be applied, the Δ area law may suggest the formation of a Δ -shaped color flux tube among the three quarks. On the other hand, Takahashi *et al.* [5,6], claimed

that the potential was described by the sum of the two-body Coulombic terms and the three-body linear term, where the latter is proportional to the Y distance with a junction at the Fermat-Torricelli point of a triangle spanned by the three quarks. This may then be called the Y area law, suggesting the formation of a Y -shaped color flux tube among the three quarks at long distances. The confining feature of the Y area law can be explained partly if the QCD vacuum possesses the property of dual superconductor [9,10], which are explicitly demonstrated by lattice QCD simulations in the maximally Abelian gauge [11–13]. Bissey *et al.* [14] investigated the profile of the non-Abelian action density in the three-quark system and found no Δ -shaped flux-tube structure at long distance, but the structure was not always of Y shape. Several ideas were proposed to reconcile this situation based on the effective models [15–18]. Perturbation theory may provide a guideline for solving the discrepancy [19,20], if higher order contributions are properly evaluated one after another.

In this paper, we thus revisit the determination of the three-quark potential in SU(3) lattice gauge theory at zero temperature. All of the previous lattice results were obtained by using the Wilson loop as the three-quark source, which is composed of the three temporal Wilson lines connected by the spatial Wilson lines with a junction as illustrated in Fig. 1 (left). The potential and the flux-tube profile should not depend on the path of the spatial Wilson lines and the location of the junction, but some of the earlier results seem to be affected by them especially when the temporal extent of the Wilson loop is not large enough. Clearly, it is desirable to have the precise lattice data with less statistical and systematic errors before evaluating the validity of the functional form.

Our strategy is then to use the Polyakov loop correlation function (PLCF) in the fundamental representation as the

*koma@numazu-ct.ac.jp

†koma.miho@nihon-u.ac.jp

¹Alexandrou *et al.* updated their result with technical refinements and arrived at slightly different conclusion [8].

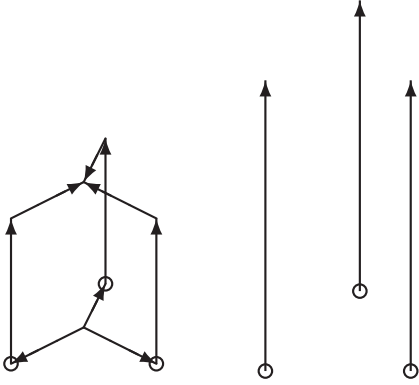


FIG. 1. The three-quark Wilson loop (left) and the three-quark PLCF (right). While the Wilson loop is composed of the three temporal Wilson lines connected by the spatial Wilson lines with a junction, the PLCF is only composed of the three Polyakov loops, where a periodic boundary condition is imposed in the time direction.

quark source. In contrast to the Wilson loop, the PLCF is free from systematic effects caused by the spatial Wilson lines, since the PLCF is composed only of the three Polyakov loops as illustrated in Fig. 1 (right), where a periodic boundary condition is imposed in the time direction. A severe problem, which is why the PLCF has not been used so far for the zero temperature simulations, may be the smallness of the expectation value in contrast to the finite temperature case [21,22], which means that ordinary simulations are ineffective as the signal is easily obscured by the statistical noise. As we demonstrate in this paper, however, this problem can be solved by employing the multilevel algorithm [23,24] with tuned simulation parameters [25]. Another reason that the PLCF has been avoided may originate from a folklore that the potential from the PLCF can contain contributions not only from the color-singlet state but also from the color-adjoint state. However, as we have demonstrated in SU(3) lattice gauge theory [26], all intermediate states of gluons equally contribute to the color-singlet potential, at least as long as one uses the PLCF in the fundamental representation (see, an illuminating discussion in Ref. [27] for SU(2) lattice gauge theory).

We obtain the three-quark potential of $O(200)$ sets of the three-quark geometries including not only the cases that three quarks are put at the vertices of acute, right, and obtuse triangles, but also the extreme cases such that three quarks are put in line. We find that most of the three-quark potentials from triangle geometries that the maximum inner angle is smaller than 120° can fall into one curve as a function of the minimal length of lines connecting the three quarks, which supports the Y -shaped flux-tube picture. From the derivative of the potential, we observe that the string tension of the three-quark potential is the same as that of the quark-antiquark potential. We also critically compare the three-quark potential to the half of the sum of the

two-body quark-antiquark potential and find a systematic deviation especially for larger triangle geometries, which brings us to a conclusion that there is certainly a force which cannot be described by the superposition of the two-body forces. We then discuss the functional form of the three-quark potential and examine its scaling behavior with respect to the lattice spacing.

This paper is organized as follows. In Sec. II, we describe how to compute the three-quark potential from the PLCF with the multilevel algorithm. We also classify various three-quark geometries. In Sec. III, we present our numerical results. Section IV is devoted to the summary of our findings. Our preliminary results have been presented at Lattice 2013 in Mainz [26], at Lattice 2014 in New York [25], and at Lattice 2015 in Kobe [28].

II. NUMERICAL PROCEDURES

In this section, we describe how to extract the three-quark potential from the PLCF and how to implement the multilevel algorithm for computing the PLCF. We then provide the definition of some practical distances and angles to classify various three-quark geometries analyzed in the present study.

A. The three-quark potential from the PLCF

We perform simulations of SU(3) lattice gauge theory (lattice QCD within the quenched approximation) in four dimensions with the lattice volume $L^3 \times T$ and the lattice spacing a by imposing periodic boundary conditions in all space-time directions. The three-quark potential is extracted from the PLCF as follows.

We first define a three-link correlator as

$$\begin{aligned} \mathbb{T}(x_0, \vec{x}_1, \vec{x}_2, \vec{x}_3)_{\alpha\beta\gamma\delta\epsilon\zeta} \\ \equiv U_4(x_0, \vec{x}_1)_{\alpha\beta} U_4(x_0, \vec{x}_2)_{\gamma\delta} U_4(x_0, \vec{x}_3)_{\epsilon\zeta}, \end{aligned} \quad (1)$$

which is a direct product of three timelike link variables $U_4(x)$ placed at a time x_0 with spatial positions of three quarks, \vec{x}_1 , \vec{x}_2 , and \vec{x}_3 . Greek indices $\alpha, \beta, \gamma, \delta, \epsilon, \zeta$ take the values from one to three, respectively. Practically, a three-link correlator is a complex matrix with $3^6 = 729$ components. The three-link correlator acts on a color state in the $\mathbf{3} \otimes \mathbf{3} \otimes \mathbf{3}$ representation of the SU(3) group $|n_{\alpha\beta\gamma}; \vec{x}_1, \vec{x}_2, \vec{x}_3\rangle$, which is an eigenstate of the Hamiltonian \mathbb{H} defined by the transfer matrix in the temporal gauge, $\mathbb{T} \equiv e^{-\mathbb{H}a}$, and then satisfies

$$\begin{aligned} \mathbb{T}(x_0, \vec{x}_1, \vec{x}_2, \vec{x}_3)_{\alpha\beta\gamma\delta\epsilon\zeta} |n_{\alpha\beta\gamma}; \vec{x}_1, \vec{x}_2, \vec{x}_3\rangle \\ = e^{-E_n(\vec{x}_1, \vec{x}_2, \vec{x}_3)a} |n_{\lambda\rho\sigma}; \vec{x}_1, \vec{x}_2, \vec{x}_3\rangle, \end{aligned} \quad (2)$$

where n is the principal quantum number and repeated Greek indices α, β, γ are to be summed over from one to three. The energies $E_n(\vec{x}_1, \vec{x}_2, \vec{x}_3)$ are positive and are

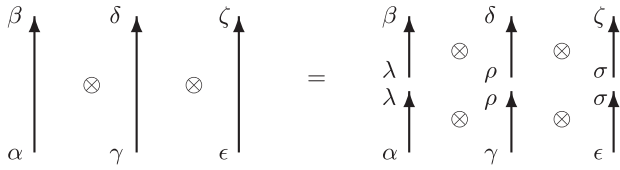


FIG. 2. A product of two three-link correlators, where repeated Greek indices λ , ρ , and σ are to be summed over from one to three.

common to all of the $3^3 = 27$ color components of $|n_{\alpha\beta\gamma}; \vec{x}_1, \vec{x}_2, \vec{x}_3\rangle$. The multiplication rule of two three-link correlators for adjacent times at x_0 and $x_0 + a$ is

$$\begin{aligned} & \{\mathbb{T}(x_0, \vec{x}_1, \vec{x}_2, \vec{x}_3)\mathbb{T}(x_0 + a, \vec{x}_1, \vec{x}_2, \vec{x}_3)\}_{\alpha\beta\gamma\delta\epsilon\zeta} \\ &= \mathbb{T}(x_0, \vec{x}_1, \vec{x}_2, \vec{x}_3)_{\alpha\lambda\gamma\rho\epsilon\sigma}\mathbb{T}(x_0 + a, \vec{x}_1, \vec{x}_2, \vec{x}_3)_{\lambda\beta\rho\delta\sigma\zeta}. \end{aligned} \quad (3)$$

With this multiplication rule a new and longer three-link correlator is created as schematically shown in Fig. 2.

We then construct the PLCF from the time-ordered product of the three-link correlators,

$$\begin{aligned} & \text{Tr}P(\vec{x}_1)\text{Tr}P(\vec{x}_2)\text{Tr}P(\vec{x}_3) \\ &= \{\mathbb{T}(0, \vec{x}_1, \vec{x}_2, \vec{x}_3)\mathbb{T}(a, \vec{x}_1, \vec{x}_2, \vec{x}_3) \\ & \quad \cdots \mathbb{T}(T - a, \vec{x}_1, \vec{x}_2, \vec{x}_3)\}_{\alpha\alpha\gamma\gamma\epsilon\epsilon}. \end{aligned} \quad (4)$$

By inserting the complete set of eigenstates,

$$\mathbf{1}_{\alpha\lambda\beta\rho\gamma\sigma} = \sum_n |n_{\alpha\beta\gamma}; \vec{x}_1, \vec{x}_2, \vec{x}_3\rangle \langle n_{\lambda\rho\sigma}; \vec{x}_1, \vec{x}_2, \vec{x}_3|, \quad (5)$$

at each time $x_0 = 0, a, \dots, T - a$, and by using the normalization condition,

$$\langle n_{\alpha\beta\gamma}; \vec{x}_1, \vec{x}_2, \vec{x}_3 | m_{\alpha\beta\gamma}; \vec{x}_1, \vec{x}_2, \vec{x}_3 \rangle = \delta_{nm}, \quad (6)$$

the expectation value of the PLCF is reduced to

$$\langle \text{Tr}P(\vec{x}_1)\text{Tr}P(\vec{x}_2)\text{Tr}P(\vec{x}_3) \rangle = \sum_{n=0}^{\infty} e^{-E_n(\vec{x}_1, \vec{x}_2, \vec{x}_3)T}. \quad (7)$$

The ground state potential, $V_{3q} \equiv E_0$, is then extracted as

$$\begin{aligned} V_{3q}(\vec{x}_1, \vec{x}_2, \vec{x}_3) &= -\frac{1}{T} \ln \langle \text{Tr}P(\vec{x}_1)\text{Tr}P(\vec{x}_2)\text{Tr}P(\vec{x}_3) \rangle \\ &+ O\left(\frac{1}{T} e^{-(E_1 - E_0)T}\right), \end{aligned} \quad (8)$$

where the terms of $O(e^{-(E_1 - E_0)T}/T)$ are always negligible at zero temperature. Therefore, once the PLCF is computed accurately for a large temporal extent T , it is straightforward to extract the ground state potential. For instance, if we refer to the value $a(E_1 - E_0) \sim 0.5$ at $\beta = 6.00$ given by Takahashi and Suganuma [29], the order of magnitude of $O(e^{-(E_1 - E_0)T}/T)$ on a lattice with $T/a = 24$, which is our

numerical setting, is estimated as $O(e^{-0.5 \cdot 24}/24) = O(10^{-7})$, which is clearly negligible compared to aV_{3q} at $\beta = 6.00$.

Note that if the sum of multiexponential functions in Eq. (7) is forcibly cast into a single exponential function, its exponent may be understood as the minus of the free energy divided by corresponding temperature. However, if the excited state contribution is negligible from the beginning and the summation in Eq. (7) is represented only by the first term with E_0 , the energy we can extract following Eq. (8) is no longer the free energy but just the ground state potential, where the notion of temperature could be irrelevant.

On the other hand, if one uses the three-quark Wilson loop as in Fig. 1 (left) with a time extent t , the expectation value will be

$$\begin{aligned} & \langle W(\vec{x}_1, \vec{x}_2, \vec{x}_3, \{\vec{x}_p\}, t) \rangle \\ &= \sum_{n=0}^{\infty} w_n(\vec{x}_1, \vec{x}_2, \vec{x}_3, \{\vec{x}_p\}, t) e^{-E_n(\vec{x}_1, \vec{x}_2, \vec{x}_3)t}, \end{aligned} \quad (9)$$

and the ground state potential is then extracted as

$$\begin{aligned} V_{3q}(\vec{x}_1, \vec{x}_2, \vec{x}_3) &= -\frac{1}{t} \ln \langle W(\vec{x}_1, \vec{x}_2, \vec{x}_3, \{\vec{x}_p\}, t) \rangle \\ &+ \frac{1}{t} \ln w_0 + O\left(\frac{1}{t} e^{-(E_1 - E_0)t}\right). \end{aligned} \quad (10)$$

The crucial difference from Eq. (8) is the presence of the nontrivial second term, since the weight factor $\{w_n\}$ is dependent not only on the temporal extent of the Wilson loop t but also on the path of the spatial Wilson lines $\{\vec{x}_p\}$. One may adopt smearing techniques [30] to the spatial links to achieve a better overlap with the ground state, $w_0 \rightarrow 1$, and then the second term can be dismissed. However, the achievement is usually incomplete especially when the interquark distance becomes larger. A possible way to overcome the incompleteness of the smearing may be to combine this technique and the variational method, although it requires a further careful look on the validity for the choice of the variational basis [8,29]. Moreover, the terms of $O(e^{-(E_1 - E_0)t}/t)$ are not easily suppressed, since t cannot be large practically. There is also limitation such as $t < T/2$ due to the periodic boundary condition in the time direction. Thus, in order to identify the first term of the r.h.s. of Eq. (10) as the ground state potential, these problems must be solved. Otherwise the contamination from the excited states cannot be avoided and the resulting potential may be overestimated, since the second term is usually negative.

B. The multilevel algorithm for the PLCF

A severe problem of the PLCF is that the expectation values of the PLCF are extremely small at zero temperature, so that they are immediately obscured by the statistical noise. By using the multilevel algorithm [23,24], however, it is possible to overcome the problem. The idea is to

compute a desired correlation function, which may have an extremely small expectation value, from the product of relatively large sublattice averages of its components (in our case it corresponds to the product of \mathbb{T} 's within a sublattice), where the sublattices are defined by dividing the lattice volume into several layers along the time direction. During the computation of the sublattice averages, the spatial links at the sublattice boundaries are kept intact. The computation of the correlation function in this way is regarded as the hierarchical functional integral method and is supported by the transfer matrix formalism of quantum field theory.

In order to make efficient use of the multilevel algorithm, it is important to choose the following two parameters appropriately. One is the number of time slices in a sublattice, $N_{\text{tsl}} = T/(aN_{\text{sub}})$, where N_{sub} is the number of sub-lattices. The other is the number of internal updates for the sub-lattice averages, N_{iupd} .

Let us explain the reason how and why the multilevel algorithm works well by looking at a simple case that the lattice volume is divided into two sublattices at the time slice $x_0 = 0$ and $x_0 = T/2$ ($N_{\text{sub}} = 2$ and $N_{\text{tsl}} = T/(2a)$). We may prepare the product of the three-link correlators $\{\mathbb{T}(0, \vec{x}_1, \vec{x}_2, \vec{x}_3) \cdots \mathbb{T}(T/2 - a, \vec{x}_1, \vec{x}_2, \vec{x}_3)\}_{\alpha\beta\gamma\delta\epsilon\zeta}$ and $\{\mathbb{T}(T/2, \vec{x}_1, \vec{x}_2, \vec{x}_3) \cdots \mathbb{T}(T - a, \vec{x}_1, \vec{x}_2, \vec{x}_3)\}_{\alpha\beta\gamma\delta\epsilon\zeta}$, and construct the PLCF by

$$\begin{aligned} & \text{Tr}P(\vec{x}_1)\text{Tr}P(\vec{x}_2)\text{Tr}P(\vec{x}_3) \\ &= \left[\mathbb{T}(0, \vec{x}_1, \vec{x}_2, \vec{x}_3) \cdots \mathbb{T}\left(\frac{T}{2} - a, \vec{x}_1, \vec{x}_2, \vec{x}_3\right) \right]_{\alpha\lambda\gamma\rho\epsilon\sigma} \\ & \quad \times \left[\mathbb{T}\left(\frac{T}{2}, \vec{x}_1, \vec{x}_2, \vec{x}_3\right) \cdots \mathbb{T}(T - a, \vec{x}_1, \vec{x}_2, \vec{x}_3) \right]_{\lambda\alpha\gamma\rho\sigma\epsilon}, \quad (11) \end{aligned}$$

where $[\cdots]$ represent taking the sublattice averages (this is not yet an expectation value). Fixing the spatial links at the sublattice boundaries may correspond to inserting two fixed sources $|\phi_1\rangle = \sum_n a_n |n_{\alpha\beta\gamma}; \vec{x}_1, \vec{x}_2, \vec{x}_3\rangle$ and $|\phi_2\rangle = \sum_n b_n |n_{\alpha\beta\gamma}; \vec{x}_1, \vec{x}_2, \vec{x}_3\rangle$ at $x_0 = 0$ and $x_0 = T/2$, respectively, where $\{a_n\}$ and $\{b_m\}$ are unknown complex values but satisfy $|a_n|^2 = |b_m|^2 = 1$ for arbitrary n . Then, Eq. (11) is evaluated, omitting arguments of the spatial vectors for simplicity, as

$$\begin{aligned} & \text{Tr}P(\vec{x}_1)\text{Tr}P(\vec{x}_2)\text{Tr}P(\vec{x}_3) \\ &= \left[|\phi_1\rangle \langle \phi_1 | \mathbb{T}(0) \cdots \mathbb{T}\left(\frac{T}{2} - a\right) \right]_{\alpha\lambda\gamma\rho\epsilon\sigma} \\ & \quad \times \left[|\phi_2\rangle \langle \phi_2 | \mathbb{T}\left(\frac{T}{2}\right) \cdots \mathbb{T}(T - a) \right]_{\lambda\alpha\gamma\rho\sigma\epsilon} \\ &= \sum_{n,m} a_m^* a_n |n_{\alpha\gamma\epsilon}\rangle \langle m_{\lambda\rho\sigma} | e^{-E_m \frac{T}{2}} \\ & \quad \times \sum_{n',m'} b_{m'}^* b_{n'} |n'_{\lambda\rho\sigma}\rangle \langle m'_{\alpha\gamma\epsilon} | e^{-E_{m'} \frac{T}{2}} \\ &= \sum_n b_n^* a_n e^{-E_n \frac{T}{2}} \cdot \sum_m a_m^* b_m e^{-E_m \frac{T}{2}}. \quad (12) \end{aligned}$$

If we take the average for a large number of different fixed sources at $x_0 = 0$ and $x_0 = T/2$ of other independent gauge configurations, we obtain the expectation value of the PLCF as in Eq. (7), since inserting many fixed sources corresponds to inserting the complete set.

It is worth noting that if $T/2$ is large enough such that the contribution from the terms of $O(e^{-(E_1 - E_0)(T/2)})$ is negligible, which is the case at zero temperature limit, Eq. (12) further reduces to

$$\begin{aligned} \text{Tr}P(\vec{x}_1)\text{Tr}P(\vec{x}_2)\text{Tr}P(\vec{x}_3) &= |a_0|^2 |b_0|^2 e^{-E_0(\vec{x}_1, \vec{x}_2, \vec{x}_3)T} \\ &= e^{-E_0(\vec{x}_1, \vec{x}_2, \vec{x}_3)T}, \quad (13) \end{aligned}$$

where $|a_0|^2 = |b_0|^2 = 1$. This means that the ground state potential E_0 can be extracted from one gauge configuration. Of course, one should be careful that the weight of one gauge configuration in the multilevel algorithm is different from that in ordinary simulations. It is important to notice that each color component of the intermediate states equally contributes to the exponential decay of the PLCF (the degeneracy is just $3^6 = 729$ in this example), and there is no dominant contribution to the potential from a particular color component, which implies that contributions from the color-singlet and color-adjoint states are the same. Equation (13) also indicates that it is possible to obtain the same gauge invariant potential even from the gauge variant PLCF constructed by selected partial intermediate states [26]. In this sense, gauge invariance of the PLCF is desirable to maximize the number of internal color statistics (the degeneracy), which may help to obtain stable values with a smaller N_{iupd} . On the other hand, if the terms of $O(e^{-(E_1 - E_0)(T/2)})$ in Eq. (12) are not small enough, the ground state potential cannot be extracted since the PLCF always suffer from contamination of excited states. In such a case, increasing the number of independent gauge configurations (statistics) does not help. Instead, the larger temporal lattice volume is needed from the beginning.

This example tells us that it is crucial to find an appropriate N_{tsl} so that the terms of $O(e^{-(E_1 - E_0)(aN_{\text{tsl}})})$ are small enough. In our experience with the standard SU(3) Wilson gauge action, there is a critical minimal length of aN_{tsl} to obtain the ground state potential. We find the value $aN_{\text{tsl}} = 0.36 \sim 0.37$ [fm] [31–33], which corresponds to $N_{\text{tsl}} = 3$ at $\beta \simeq 5.85$, $N_{\text{tsl}} = 4$ at $\beta \simeq 6.00$, and $N_{\text{tsl}} = 6$ at $\beta \simeq 6.30$. Then, the appropriate N_{iupd} is chosen by looking at the convergence history of the PLCF as a function of N_{iupd} . If one is interested in the behavior of the potential at long distances, the larger N_{iupd} is needed.

C. The classification of various three-quark geometries

We compute the PLCF composed of the three Polyakov loops, $\text{Tr}P(\vec{x}_1)\text{Tr}P(\vec{x}_2)\text{Tr}P(\vec{x}_3)$, where the spatial locations of the Polyakov loops, \vec{x}_1 , \vec{x}_2 , and \vec{x}_3 correspond to those of three quarks in the three-dimensional space, respectively. As shown in Fig. 3, there are five types of three-quark

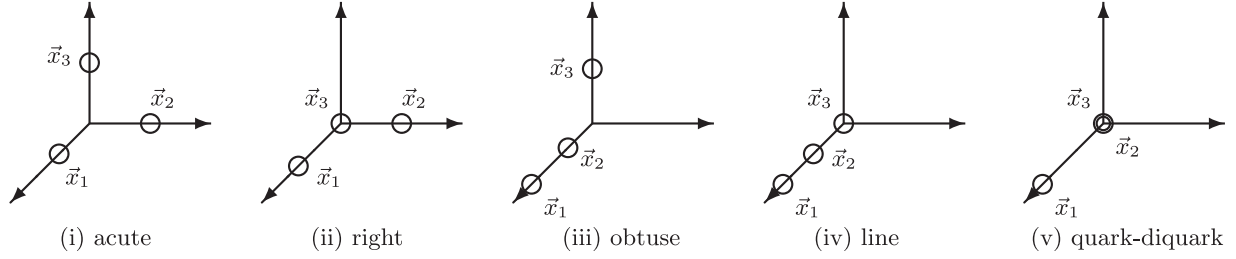


FIG. 3. The three-quark geometries investigated in our numerical simulations. The circles represent the spatial location of quarks. Three Polyakov loops are put at the vertices of (i) acute, (ii) right, (iii) obtuse triangles, and are also put in (iv) line, and are put to be (v) the quark-diquark system.

geometries: three quarks are put at the vertices of acute (ACT), right (RGT), obtuse (OBT) triangles, and are put in line (LIN). As a special case, two of three quarks are put at the same location, which corresponds to a quark-diquark system (QDQ).

These three-quark geometries can be classified by the value of the maximum inner angle of a triangle

$$\begin{aligned} \theta_{\max} &= \max(\theta_1, \theta_2, \theta_3) \\ &= \cos^{-1} \left(\frac{r_{\max}(r_1^2 + r_2^2 + r_3^2 - 2r_{\max}^2)}{2r_1 r_2 r_3} \right), \end{aligned} \quad (14)$$

where

$$r_1 = |\vec{x}_2 - \vec{x}_3|, \quad r_2 = |\vec{x}_3 - \vec{x}_1|, \quad r_3 = |\vec{x}_1 - \vec{x}_2|, \quad (15)$$

are interquark distances and $r_{\max} = \max(r_1, r_2, r_3)$ (see, Fig. 4). Acute triangles satisfy $\theta_{\max} < 90^\circ$, which contain equilateral and isosceles triangles in our study. Right triangles are the case $\theta_{\max} = 90^\circ$. Obtuse triangles are further classified into two types depending on θ_{\max} , obtuse-narrow (OBTN) triangles for $90^\circ < \theta_{\max} < 120^\circ$ and obtuse-wide (OBTW) triangles for $120^\circ \leq \theta_{\max} < 180^\circ$.

In contrast to the classification of the three-quark geometries, the parametrization of the three-quark potential is not straightforward. This is due to the fact that the potential can depend not only on the location of three quarks, \vec{x}_1 , \vec{x}_2 , and \vec{x}_3 , but also on the structure of the flux tube spanned among the three quarks, which is unknown *a priori* because of the nonperturbative feature of the QCD vacuum. Therefore, the determination of the functional form of the potential is nothing but the finding of appropriate distances that can capture the systematic behavior of the potential. Such distances should be symmetric under the permutation of the quark positions.

The simplest distance is then given by the sum of interquark distances in Eq. (15),

$$\Delta = r_1 + r_2 + r_3. \quad (16)$$

Another possible distance is given by the minimal total length of lines connecting the three quarks via the Fermat-Torricelli point of a triangle,

$$Y = \sqrt{\frac{r_1^2 + r_2^2 + r_3^2 + 4\sqrt{3}S}{2}}, \quad (17)$$

where S is the area of the triangle given by Heron's formula,

$$s = \frac{1}{2}\Delta, \quad S = \sqrt{s(s-r_1)(s-r_2)(s-r_3)}. \quad (18)$$

Note that the distance between the Fermat-Torricelli point and each vertex is

$$l_i = Y - \frac{1}{Y} \left(r_i^2 + \frac{4S}{\sqrt{3}} \right). \quad (19)$$

For finding the location of the Fermat-Torricelli point the method presented in [34,35] may be useful.

In fact, these two types of distances, Δ and Y , were often used to examine the behavior of the potential in the earlier studies. We also follow them in our analyses of the three-quark potential. In terms of the minimal length of connected lines, Y is reduced to

$$\Lambda = \Delta - r_{\max}, \quad (20)$$

when $\theta_{\max} \geq 120^\circ$. It is then convenient to introduce a combined distance of Y and Λ classified by θ_{\max} as

$$L_{\text{str}} = \begin{cases} Y & (\theta_{\max} < 120^\circ) \\ \Lambda & (\theta_{\max} \geq 120^\circ) \end{cases}. \quad (21)$$

For a detailed comparison with the quark-antiquark potential, we also use a reduced interquark distance R defined by

$$\frac{1}{R} = \frac{1}{r_1} + \frac{1}{r_2} + \frac{1}{r_3}, \quad (22)$$

and an averaged distance between the Fermat-Torricelli point and three sides of a triangle (see, Fig. 4),

$$h = \frac{1}{3}(h_1 + h_2 + h_3), \quad (23)$$

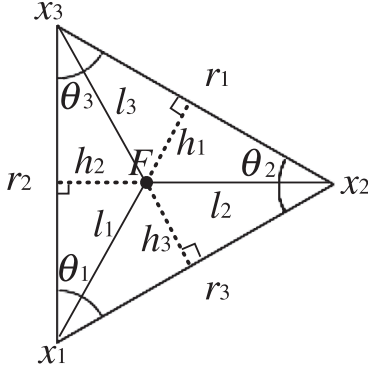


FIG. 4. The definition of distances and angles of a triangle used in our analyses: x_i denotes the location of i th quark, F the Fermat-Torricelli point, so that $\angle x_1 F x_2 = \angle x_2 F x_3 = \angle x_3 F x_1 = 120^\circ$. h_i denotes the distance between F and each side. Δ and Y are given by $\Delta = r_1 + r_2 + r_3$ and $Y = l_1 + l_2 + l_3$, respectively.

where

$$h_i = \frac{2S_i}{r_i} = \frac{\sqrt{3}l_j l_k}{2r_i} \quad (i, j, k: \text{cyclic}). \quad (24)$$

Note that $S_i = (1/2)l_j l_k \sin 120^\circ$ is the area of the triangle spanned by three points x_j , x_k , and F .

As we will see in the next section, these distances are quite useful to see the systematic behaviors of the three-quark potential, although it may be possible to define other symmetric distances [16].

III. NUMERICAL RESULTS

In this section, we present results of our lattice Monte Carlo simulations. We emphasize that the crucial difference of our simulations from the earlier ones of other groups is that we compute the three-quark potential from the PLCF, which could provide us with numerical results with less systematic effects than that from the Wilson loop.

We carried out Monte Carlo simulations using the standard Wilson gauge action in SU(3) lattice gauge theory. The basic simulation parameters are summarized in Table I. The lattice spacing was determined by the Sommer scale $r_0 = 0.50$ [fm] [36]. One Monte-Carlo update consisted of one heat-bath and five over-relaxation steps. The gauge coupling β and the lattice volume $L^3 \times T$ were chosen to make maximal use of the multilevel algorithm within our computer resource.

TABLE I. The basic simulation parameters used in this study. The numbers of internal updates N_{iupd} and of the gauge configurations N_{cnf} are dependent on the observables.

$\beta = 6/g^2$	$(L/a)^3(T/a)$	a [fm]	N_{sub}	N_{tsl}
5.85	24^4	0.123	8	3
6.00	24^4	0.093	6	4
6.30	24^4	0.059	4	6

In fact, we once investigated the quark-antiquark potential from the PLCF at $\beta = 6.00$ for various lattice volumes including 16^4 , 20^4 , and $20^3 \times 40$ using the multilevel algorithm [32,33], and found no noticeable dependence on the temporal size T . Therefore, our results of the three-quark potential on the 24^4 lattice at $\beta = 6.00$ are also expected to be independent of T , and can be regarded as those at zero temperature. Note that the lattice volume 24^4 at $\beta = 5.85$ and $\beta = 6.30$ approximately corresponds to 32^4 and 16^4 at $\beta = 6.00$, respectively.

The numbers of internal updates N_{iupd} and of the gauge configurations N_{cnf} are dependent on the observables, which will be described in the following subsections individually. The special attention is paid to the data from one gauge configuration at $\beta = 6.00$, which has no statistical error. On the other hand, the data with statistical errors are from a certain number of gauge configurations, and the corresponding errors are estimated by the standard jackknife method. When we perform the χ^2 fit, we mainly use the data with statistical errors.

A. The potential from one gauge configuration

At the beginning, we demonstrate that the three-quark potential can be obtained from one gauge configuration by tuning the parameters of the multilevel algorithm as explained in Sec. II B. In Fig. 5, we plot typical convergence histories of the PLCF for the equilateral triangle configurations of one gauge configuration at $\beta = 5.85$ ($N_{\text{tsl}} = 3$), $\beta = 6.00$ ($N_{\text{tsl}} = 4$), and $\beta = 6.30$ ($N_{\text{tsl}} = 6$) as a function of the number of internal updates N_{iupd} . We find that the fluctuation of the PLCF is washed out and the values become stable as we increase N_{iupd} . Required N_{iupd} for convergence depends on the size of the triangle.

Once the PLCF becomes stable, it can be regarded as the expectation value as in Eq. (13), and then the potential is computed by Eq. (8). In Fig. 6, we show the potential at $\beta = 6.00$ from one gauge configuration at $N_{\text{iupd}} = 500000$ as a function of Y defined in Eq. (17). The potential is also compared to that from the average of $N_{\text{cnf}} = 9$ independent gauge configurations (the number 9 is just the maximum gauge configurations that we obtained within our available computer resources). The numerical error of the average is estimated by the standard jackknife method. It is obvious that the potential is determined accurately, where the potential from one gauge configuration already represents the average. The level of agreement between the two potentials can be quantified by evaluating the relative error $(V_{3q}^{(\text{ave})} - V_{3q})/V_{3q}^{(\text{ave})}$, which is plotted in Fig. 7. This figure shows that the relative error is gradually increasing at large Y , which is one of the origin of the statistical error of the average. However it is only 0.8% even at a quite long distance $Y/a \approx 18$.

The fit of the averaged potential to an empirical functional form,

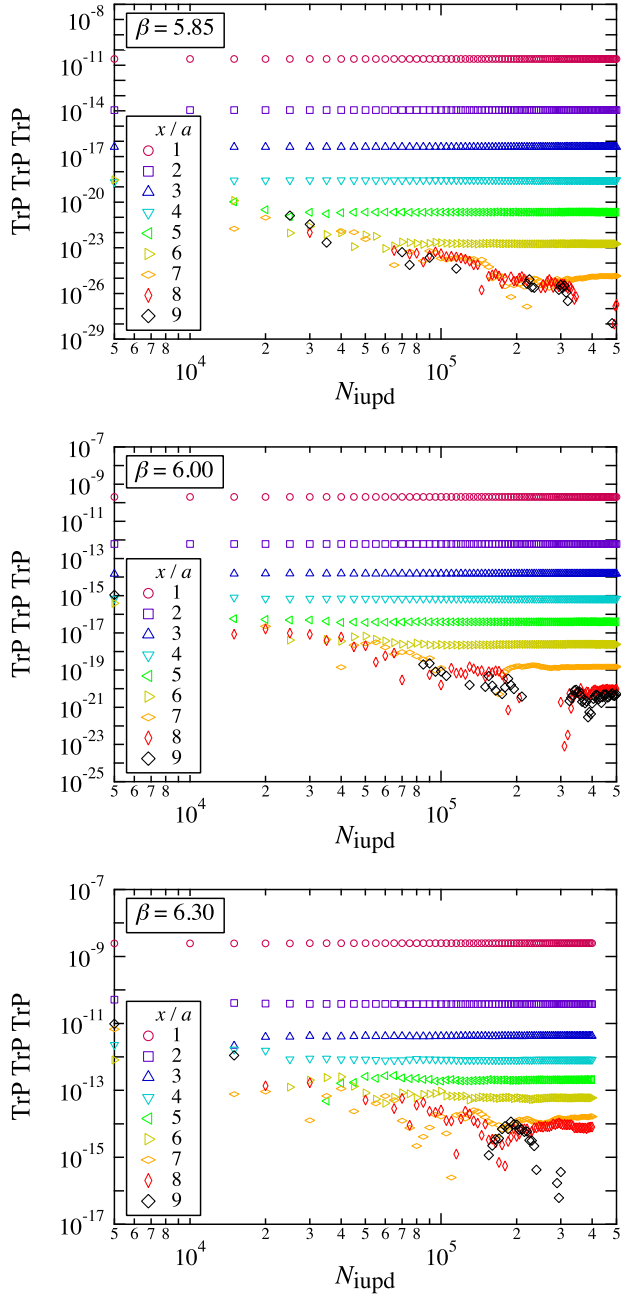


FIG. 5. Convergence histories of the PLCF of the equilateral triangle geometries at $\beta = 5.85$ (upper), $\beta = 6.00$ (middle), and $\beta = 6.30$ (lower) as a function of N_{iupd} , where quarks are placed at $(x, 0, 0)$, $(0, x, 0)$, and $(0, 0, x)$.

$$V_{3q}^{(Y)} = -\frac{A_{3q}^{(Y)}}{Y} + \sigma_{3q}Y + \mu_{3q}, \quad (25)$$

yields $A_{3q}^{(Y)} = 0.662(6)$, $\sigma_{3q}a^2 = 0.0446(3)$, and $\mu_{3q}a = 1.092(3)$, which describes the behavior of the data nicely as shown in Fig. 6. It is interesting to note that the coefficient in front of Y , which we may call the three-quark string tension σ_{3q} , is consistent with the string tension of the

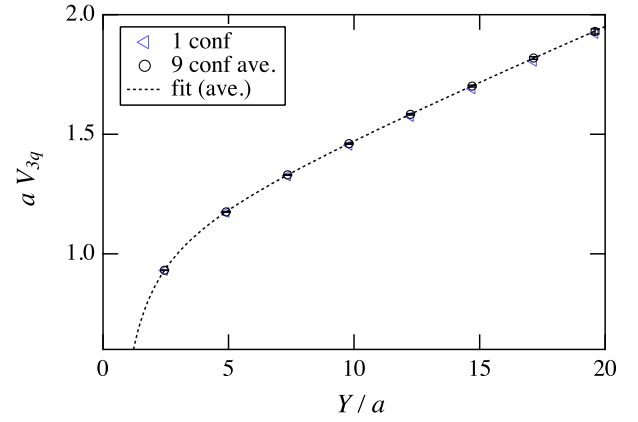


FIG. 6. The three-quark potentials of the equilateral triangle geometries at $\beta = 6.00$ obtained from one gauge configuration and from the average of 9 gauge configurations as a function of Y . The dotted line represents the fit curve to the averaged potential.

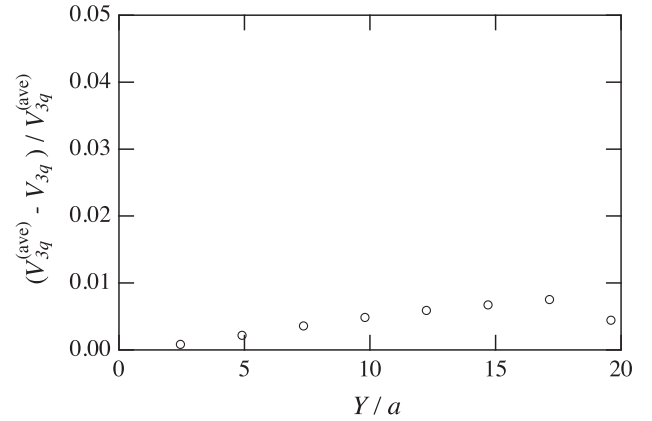


FIG. 7. The relative error between the two potentials in Fig. 6, $(V_{3q}^{(ave)} - V_{3q})/V_{3q}^{(ave)}$.

quark-antiquark potential $\sigma_{q\bar{q}}$. In addition, the constant term μ_{3q} is approximately $(3/2)\mu_{q\bar{q}}$, where $\mu_{q\bar{q}}$ is the constant term of the quark-antiquark potential (discussed later in Sec. III E).

B. The potential of various three-quark geometries

We then extend the computation of the potential to various three-quark geometries as in Fig. 3 by using the same one gauge configuration at $\beta = 6.00$. In total we investigate 221 three-quark geometries as summarized in Table II. We list all of these potential data within the significant digits in Appendix A.

In Fig. 8, we plot all the potential data against Δ and L_{str} defined in Eqs. (16) and (21). At glance, we find that neither Δ nor L_{str} can provide a universal functional form of the three-quark potential, since all the data do not fall into one curve with these distances. However, if we look at the potential of ACT, RGT, and OBTN against L_{str} carefully and restrict the data only for $r_{\text{min}}/a > 2$, where

TABLE II. The number of various three-quark geometries investigated from one gauge configuration at $\beta = 6.00$ (total 221). The potential data are summarized in tables in Appendix A.

Classification (abbr.)	Count	Table
acute (ACT)	68	III
right (RGT)	43	IV
obtuse-narrow (OBTN)	27	V
obtuse-wide (OBTW)	28	VI
line (LIN)	32	VII
quark-diquark (QDQ)	23	VIII

$r_{\min} = \min(r_1, r_2, r_3)$, by assuming that they do not suffer from severe lattice cutoff effects, we observe an excellent linearly-rising behavior as explicitly shown in Fig. 9. As we will demonstrate in the following analysis, the corresponding string tension is consistent with that of the quark-antiquark potential.

The behavior of the potentials of OBTW and LIN is not as clear as that of ACT and RGT. They are not on a simple

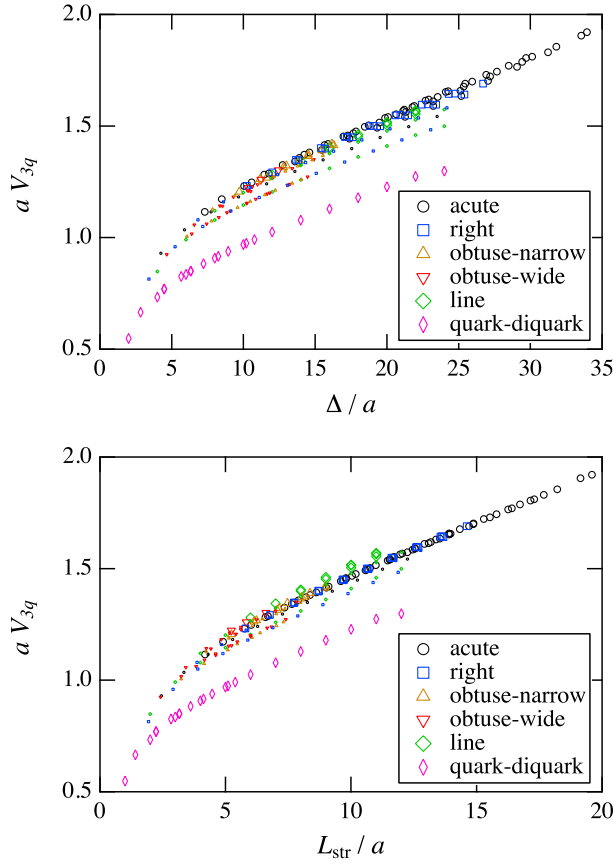


FIG. 8. The three-quark potential against Δ defined in Eq. (16) (upper) and L_{str} defined in Eq. (21) (lower). Smaller markers denote data from the geometries for $r_{\min}/a \leq 2$, which may suffer from lattice cutoff effects.

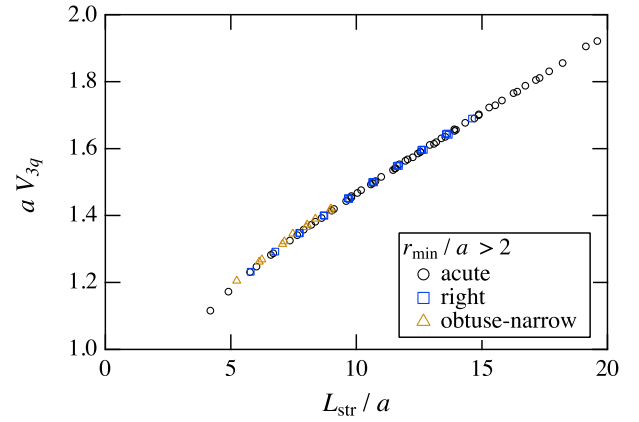


FIG. 9. The three-quark potential of acute, right, and obtuse-narrow geometries restricted to $r_{\min}/a > 2$ against L_{str} .

function of L_{str} . In particular, as explicitly shown in Fig. 10 for LIN, the potentials are dependent also on r_{\min} . The increasing behaviors as a function of r_{\min} are similar with each other, which in turn imply that the three quarks in LIN prefers to be QDQ. As clarified later in Sec. III D, the potential for LIN is well described by the half of the sum of the quark-antiquark potential, so that the interval between the potentials for various L_{str} in Fig. 10 is approximately given by $\sigma_{q\bar{q}}\delta L_{\text{str}}$, where δL_{str} is the difference of L_{str} .

The potential of QDQ exhibits a different behavior from that of other three-quark geometries. In Fig. 11, we plot the QDQ potential (we have selected only on-axis data), which is then compared to the quark-antiquark potential with the same distance between a quark and an antiquark r (the raw data of the quark-antiquark potential are summarized in Table XI in Appendix B). It appears that the two potentials are almost the same. Fitting the two potentials to the functional form,

$$V = -\frac{A}{r} + \sigma r + \mu, \quad (26)$$

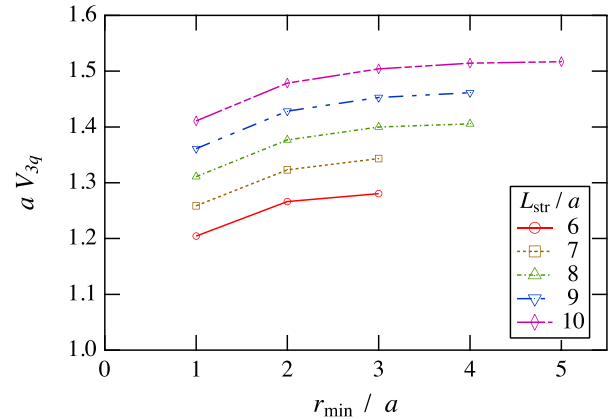


FIG. 10. The three-quark potential of line geometries against r_{\min} .

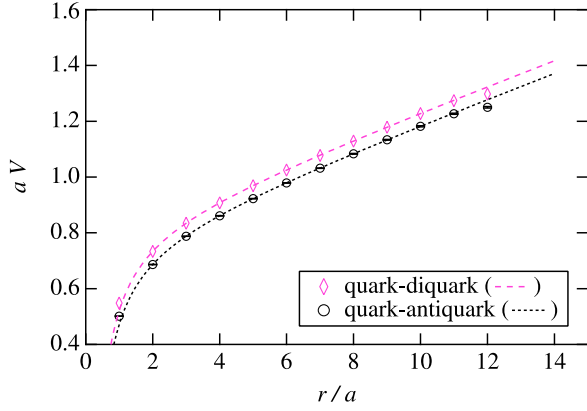


FIG. 11. The quark-diquark and quark-antiquark potentials against r . The dashed and dotted lines are the fit curves to Eq. (26), respectively.

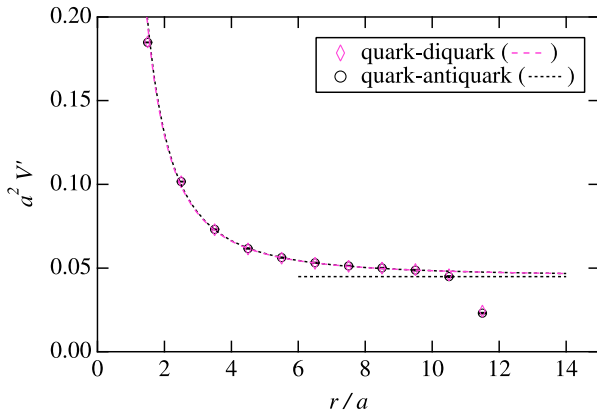


FIG. 12. The derivatives of the quark-diquark and quark-antiquark potentials with respect to r . The horizontal dotted line corresponds to the string tension of the quark-antiquark potential $\sigma_{q\bar{q}}a^2 = 0.0449$ (see, Table XII).

leads to the values $A_{qdq} = 0.336(2)$, $\sigma_{qdq}a^2 = 0.0449(1)$, and $\mu_{qdq}a = 0.811(1)$ for the QDQ potential,² while $A_{q\bar{q}} = 0.340(2)$, $\sigma_{q\bar{q}}a^2 = 0.0449(2)$, and $\mu_{q\bar{q}}a = 0.766(1)$ for the quark-antiquark potential (see, Table XII in Appendix B), where subscripts are added to distinguish the fit results; two potentials are consistent with each other except for the constant shift, $a(\mu_{qdq} - \mu_{q\bar{q}}) = 0.045(3)$.

We also compute the derivatives of the QDQ and the quark-antiquark potentials with respect to r , which are shown in Fig. 12. We find that the two results completely agree with each other, including a systematic effect caused by finite volume. These results mean that reduction of the representation in SU(3) color group, $\mathbf{3} \otimes (\bar{\mathbf{3}} \oplus \mathbf{6}) \Rightarrow \mathbf{3} \otimes \bar{\mathbf{3}}$, is realized nonperturbatively. Note that a similar

²The errors of the QDQ data, which are absent because of $N_{\text{cnf}} = 1$, are estimated from the residuals in the fitting process, and are used to evaluate the errors of the fit parameters.

result is obtained in Ref. [37] by using the T -shaped three-quark Wilson loop, where the distance between the two quarks for the diquark is set to two lattice steps.

C. The string tension of the flux tube

The analysis in Sec. III B indicates that all of the three-quark potentials of various three-quark geometries cannot be parametrized by a unique distance simultaneously. However, if we look at the three-quark potential plotted in Fig. 8 optimistically, especially the plot against L_{str} , there seems to be a common increasing behavior with different constant shifts. This may probably be due to the fact that somehow a common type of flux tube is formed among three quarks to minimize the total energy of the three-quark system, while the difference of the constants originates only from short distance effects among the three quarks, which persists even if one of the three quarks is located at a distance. We thus investigate the derivative of the potential with respect to L_{str} so that the short distance effects can be removed from the potential.

Let us first focus on the potential of the isosceles triangle geometries within ACT, where the two of three quarks are placed at $\vec{x}_1 = (x, 0, 0)$ and $\vec{x}_2 = (0, x, 0)$, and the remaining third quark is placed at $\vec{x}_3 = (0, 0, z)$ with $z \geq x$. In this case, L_{str} is identical to Y and the distance between the Fermat-Torricelli point and \vec{x}_1 and \vec{x}_2 , respectively, is the same $l_1 = l_2 = (\sqrt{6}/3)x$ (see, Fig. 4). Therefore, pulling the third quark (changing z) with the fixed first and second quarks does not affect the location of the Fermat-Torricelli point, which just affects the increase of the energy between the Fermat-Torricelli point and the third quark, where $l_3 = \sqrt{z^2 + x^2/2} - x/\sqrt{6}$. We then compute the derivative of the potential with respect to Y for several fixed values of x ,

$$V'_{3q} = \frac{V_{3q}(x, z + \delta z) - V_{3q}(x, z)}{\delta Y}. \quad (27)$$

In Fig. 13 (upper), we plot the result for one gauge configuration at $\beta = 6.00$ with the classification in terms of the distance between the first and second quarks, $r_{\text{min}} = \sqrt{2}x$, where $x/a = 1, 2, \text{ and } 3$ (in this case, $\delta Y = \delta l_3$). We find that all the derivatives behave quite similarly and approach a constant value at long distance. Remarkably, the constant value is nothing but the string tension in the quark-antiquark system, $\sigma_{q\bar{q}}a^2 = 0.0449$ (see, Table XII). Since the third quark is chosen arbitrarily among the three, this result also supports a picture of the Y -shaped flux-tube formation. This feature agrees with that was pointed out by Takahashi *et al.* [5,6] based on the χ^2 fit to the potential data with the Y Ansatz.

We then pay attention to the potentials of RGT, where $\vec{x}_2 = (0, y, 0)$ and $\vec{x}_3 = (0, 0, 0)$, and the remaining first quark is placed at $\vec{x}_1 = (x, 0, 0)$, where $x \geq y$. In this case,

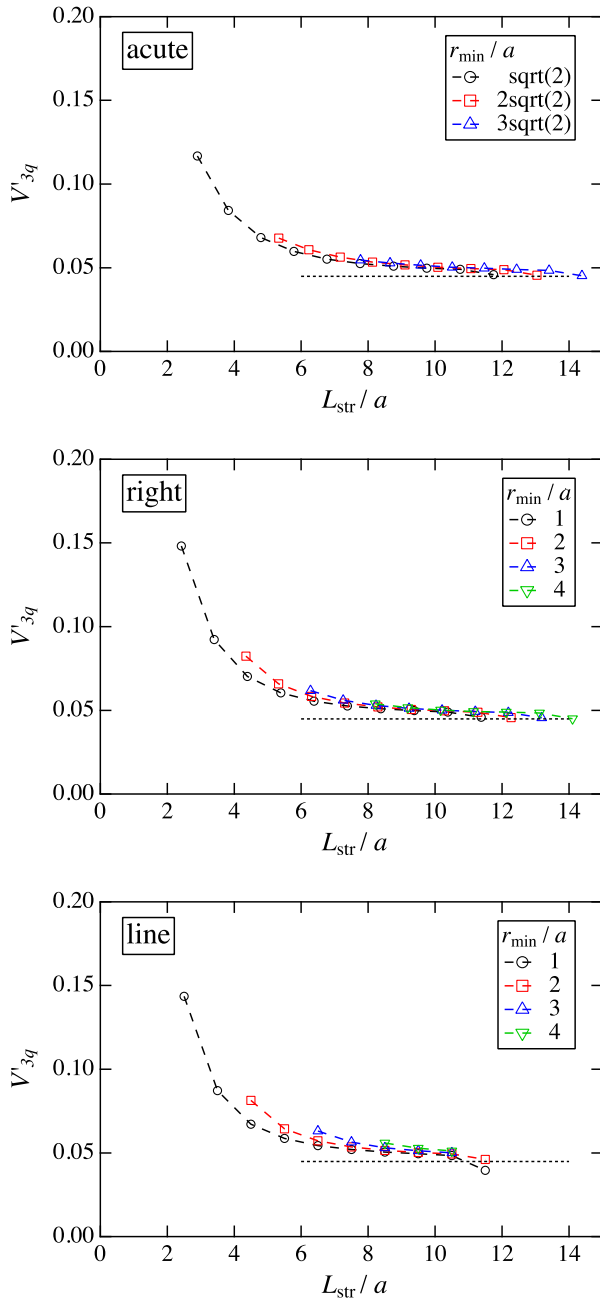


FIG. 13. The derivatives of the three-quark potential with respect to L_{str} for acute (upper), right (middle), and line (lower) geometries. The dotted line in each plot corresponds to the string tension of the quark-antiquark potential $\sigma_{q\bar{q}}a^2 = 0.0449$ (see Table XII).

although the location of the Fermat-Torricelli point is slightly dependent on changing x , it becomes insensitive to x when $x \gg y$. The derivative is then defined by

$$V'_{3q} = \frac{V_{3q}(x + \delta x, y) - V_{3q}(x, y)}{\delta Y}. \quad (28)$$

In Fig. 13 (middle), we plot the result for the same one gauge configuration with the classification in terms of the

distance between the second and third quarks, $r_{min} = y$, where $y/a = 1 \sim 4$. We find that all the derivatives approach the constant value, $\sigma_{q\bar{q}}a^2 = 0.0449$, at long distance: the tendency is quite the same as that for ACT.

We finally examine the potentials of LIN, where $\vec{x}_1 = (x_1, 0, 0)$, $\vec{x}_2 = (x_2, 0, 0)$, and $\vec{x}_3 = (0, 0, 0)$, which is an extreme case that there is probably no chance to form a junction of the flux tube. For a fixed distance $r_{min} = x_2$ ($0 < x_2 < x_1/2$), the derivative is then defined by

$$V'_{3q} = \frac{V_{3q}(x_1 + \delta x_1, x_2) - V_{3q}(x_1, x_2)}{\delta x_1}. \quad (29)$$

In Fig. 13 (bottom), we plot the result for the same one gauge configuration as a function of $L_{str} = x_1$. We again find that all the derivatives approach the constant value, $\sigma_{q\bar{q}}a^2 = 0.0449$, at long distance.

These results strongly indicate that the energy of the flux tube per unit length, the string tension, is common to that of the quark-antiquark potential regardless of the geometry of three quarks.

D. Detailed comparison with the two-body quark-antiquark potential

In the earlier studies of the three-quark potential, there was a claim that the potential was described by the half of the sum of two-body potentials in the quark-antiquark system [4,7]. However, our results in Sec. III C, indicating the presence of the flux-tube junction in larger ACT and RGT, clearly contradict the earlier claim. Thus we critically compare the three-quark potential with the quark-antiquark potential. In fact, this is possible only when the both potentials are determined accurately up to long distance, otherwise one cannot distinguish the difference between them since it is not so apparent in practice as we will see below.

In Fig. 14, we plot the relative error between the three-quark potential and the half of the sum of the quark-antiquark potentials at $\beta = 6.00$,

$$\frac{\delta V}{V_{3q}} = \frac{1}{V_{3q}} \left(V_{3q}(\vec{x}_1, \vec{x}_2, \vec{x}_3) - \frac{1}{2} \sum_{i=1}^3 V_{q\bar{q}}(r_i) \right), \quad (30)$$

against Δ defined in Eq. (16), where we have selected only 55 three-quark geometries out of 221 ones. The selection is to perform the subtraction in Eq. (30) by using only the available raw data of the quark-antiquark potential as summarized in Tables XI and XIII in Appendix B. We have avoided the use of the fit function of the quark-antiquark potential in Eq. (26), which may cause unwanted systematic effects especially at short distance.

We observe that the relative error is almost constant about 0.003 at $\Delta/a < 10$, which may be understood as zero within the systematic error due to the use of different gauge

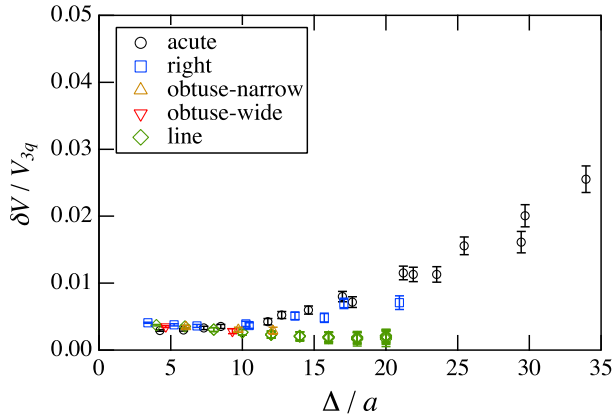


FIG. 14. The relative error between three-quark potential and the half of the sum of the quark-antiquark potential, $\delta V/V_{3q}$ against Δ defined in Eq. (16). As the three-quark potential is from one gauge configuration with no statistical error, the error bars in this plot are purely from that of the quark-antiquark potential from $N_{\text{cnf}} = 20$ (see Tables XI and XIII).

configurations,³ where the three-quark potential is from one gauge configuration with $N_{\text{iupd}} = 500000$, while the quark-antiquark potential is from $N_{\text{cnf}} = 20$ gauge configurations with $N_{\text{iupd}} = 100000$. On the other hand, the difference becomes apparent at $\Delta/a > 10$ especially for ACT and RGT, both of which show a similar increasing behavior up to 0.03 at $\Delta/a = 35$. Note that the relative error 0.03 is already large enough compared to that from the gauge configuration dependence as demonstrated in Fig. 7. In Fig. 15, we also plot the same relative error in Eq. (30) against θ_{max} defined in Eq. (14). Clearly, some of ACT and RGT data (correspond to larger Δ) exhibit a large deviation from zero.

The above two results seem to indicate that the large deviation in ACT and RGT originates from the formation of the flux-tube junction, since only these configurations are possible to form a proper junction at larger triangle. On the other hand, even in ACT and RGT, the flux-tube junction cannot be formed properly when the size of the triangle is insufficient. It seems that there is a critical size of the triangle to form a proper flux-tube junction. Based on this expectation, in Fig. 16, we then plot the relative error in Eq. (30) against the distance h defined in Eq. (23), the averaged distance between the Fermat-Torricelli point and three sides of a triangle. Note that $h = 0$ for LIN, while $h > 0$ for the other triangles. We find that the relative errors of all the three-quark potential are well parametrized by h .

³Note, however, that our further analysis using exactly the same $N_{\text{cnf}} = 200$ gauge configurations for the three-quark and the quark-antiquark potentials at $\beta = 6.00$ with $N_{\text{iupd}} = 10000$ indicates that this constant still remains finite about 0.002, which may be due to lattice cutoff effects. These potentials are not presented in this paper as the number of geometries is very limited, but the data are available on request.

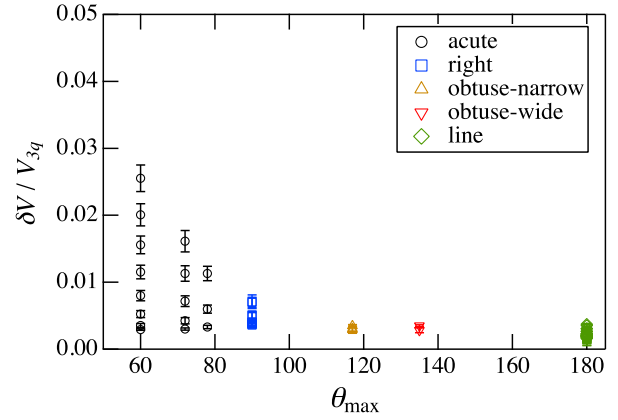


FIG. 15. The same plot as in Fig. 14, but against θ_{max} defined in Eq. (14).

The dashed line corresponds to a fit curve for the ACT data, which is an empirical quadratic function given by

$$\frac{\delta V}{V_{3q}} = c_0 + c_1(h/a) + c_2(h/a)^2, \quad (31)$$

where $c_0 = 0.0029(3)$, $c_1 = -0.0011(7)$, and $c_2 = 0.0026(3)$. The relative errors seem to start increasing around $h/a \sim 0.6$.

The difference between the three-quark potential and the half of the sum of the quark-antiquark potentials signals an existence of three-body force among the three quarks. Our results in this subsection indicate that the difference is not so drastic when the size of the triangle is small or θ_{max} approaches 180°, while it shows up gradually for larger ACT and RGT. In other words, it seems that the emergence of the three-body effects depends on whether the inter-quark distance among three quarks is large enough to form a flux-tube junction inside the triangle.

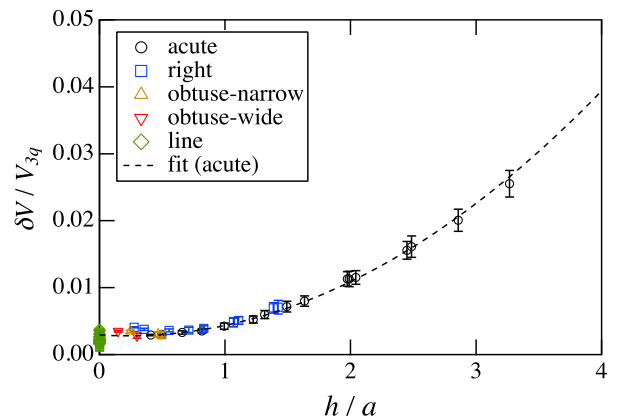


FIG. 16. The same plot as in Fig. 14, but against h defined in Eq. (23). The fit curve is given by Eq. (31).

E. The functional form of the three-quark potential

The analysis in Sec. III C suggests that the long distance part of the three-quark potential can be described by the term $\sigma_{3q}L_{\text{str}}$, where the coefficient σ_{3q} is common to that of the quark-antiquark potential $\sigma_{q\bar{q}}$. In addition, a naive fit result of the three-quark potential of the equilateral triangle geometries in Sec. III A as well as the analysis in Sec. III D have indicated that the potential also contains a constant term, which is approximately 3/2 of that in the quark-antiquark potential $\mu_{q\bar{q}}$. The presence of such a constant term in the three-quark potential is quite natural in terms of the self-energy of quarks, which will be proportional to the number of quarks involved in the system.

We then investigate the behavior of the rest of the potential by subtracting the confinement term $\sigma_{q\bar{q}}L_{\text{str}}$ and an expected constant term $(3/2)\mu_{q\bar{q}}$ from the three-quark potential,

$$V_{3q}^{(\text{sub}1)} = V_{3q} - \left(\sigma_{q\bar{q}}L_{\text{str}} + \frac{3}{2}\mu_{q\bar{q}} \right), \quad (32)$$

which will be useful to clarify the short distance part of the potential. In Fig. 17, we plot Eq. (32) against R defined in Eq. (22), where the three-quark potential used in this analysis is the same as that used in the previous subsections at $\beta = 6.00$. From the quark-antiquark potential we take the values $\sigma_{q\bar{q}}a^2 = 0.0449(2)$ and $\mu_{q\bar{q}}a = 0.766(1)$ (see Table XII in Appendix B). Remarkably, we find two systematic curves⁴: one is mostly for LIN and the other is for triangle geometries although both seem to overlap at $R/a < 1$. The data of LIN are well described by a function $-A_{q\bar{q}}/(2R)$ (the dotted line in the figure), where $A_{q\bar{q}} = 0.340(2)$ is also from Table XII, which may not be surprising after the analysis in Sec. III D. Since $L_{\text{str}} = \Delta/2$ for LIN, the difference of the potential from the half of the sum of the quark-antiquark potential is at most 0.3% relative error as explicitly shown in Fig. 14. What we should pay attention to is then the behavior of the other data for triangle geometries, which clearly deviates from the function $-A_{q\bar{q}}/(2R)$. Moreover, it seems that the curve approaches a negative constant value at large R . We then perform an empirical χ^2 fit to the functional form,

$$V_{3q}^{(\text{R})} = -\frac{A_{3q}^{(\text{R})}}{R} + \tilde{\mu}_{3q}, \quad (33)$$

which yields $A_{3q}^{(\text{R})} = 0.126(3)$ and $\tilde{\mu}_{3q}a = -0.062(4)$ with $\chi^2/N_{\text{df}} = 0.04$, where the averaged potential of the equilateral triangle configuration with error bars is taken into account in the fit. It turns out that Eq. (33) nicely captures the increasing behavior of $V_{3q}^{(\text{sub}1)}$ (the dashed line in the figure). We find that $A_{3q}^{(\text{R})}$ is significantly smaller than $A_{q\bar{q}}/2 = 0.170$ about 26%, namely,

⁴Although we attempted to plot $V_{3q}^{(\text{sub}1)}$ with Δ and L_{str} , we failed to see any systematic behaviors.

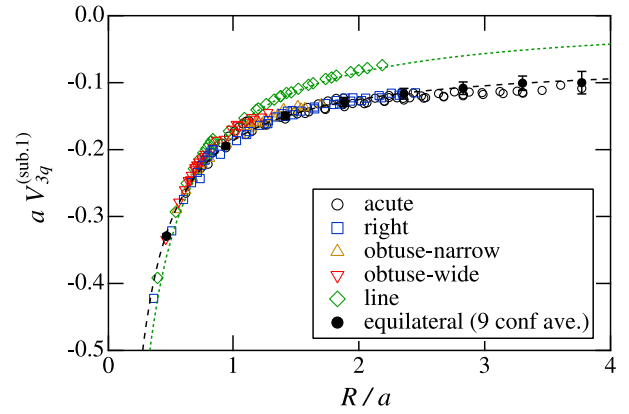


FIG. 17. The three-quark potential after subtracting the confinement and constant terms $V_{3q}^{(\text{sub}1)}$ in Eq. (32) against the reduced distance R defined in Eq. (22). The open symbols are the three-quark potential from one gauge configuration at $\beta = 6.00$, and the filled circles with error bars are from 9 gauge configurations of the equilateral triangle geometries. The dotted line corresponds to $-A_{q\bar{q}}/(2R)$, and the dashed line the fit curve given by Eq. (33).

$$A_{3q}^{(\text{R})} = \frac{A_{q\bar{q}}}{2} (1 - 0.259), \quad (34)$$

and $\tilde{\mu}_{3q}$ has a negative value as expected. The value 0.259 may be further tuned by performing a more sophisticated fit. The absolute value of $\tilde{\mu}_{3q}$ is one order of magnitude smaller than $\mu_{q\bar{q}}$, but still seems to be finite.

One may suspect at this stage that the existence of $\tilde{\mu}_{3q}$ just reflects a lattice artifact at $\beta = 6.00$, however, the following analysis in Sec. III F shows a kind of scaling behavior on $\tilde{\mu}_{3q}$, which implies that $\tilde{\mu}_{3q}$ reflects a physical effect. Since the negative shift of the energy at large R appears only for triangle geometries, we speculate that it just represents an energy reduction due to formation of the flux-tube junction. Of course, if this is the case, the energy reduction could depend on the size of the triangle. This feature seems to be incorporated effectively by rewriting Eq. (33) as

$$V_{3q}^{(\text{R})} = -\frac{A_{q\bar{q}}}{2R} + \left(0.259 \cdot \frac{A_{q\bar{q}}}{2R} + \tilde{\mu}_{3q} \right), \quad (35)$$

where the first term purely represents two-body interaction between quarks while the terms inside parenthesis are interpreted as the three-body junction effect. In Fig. 18, we plot

$$V_{3q}^{(\text{sub}2)} = V_{3q} - \left(-\frac{A_{q\bar{q}}}{2R} + \sigma_{q\bar{q}}L_{\text{str}} + \frac{3}{2}\mu_{q\bar{q}} \right), \quad (36)$$

against R . Although it is not obvious in Fig. 17 whether OBTW belongs to LIN or triangle category, the plot in Fig. 18 seems to support the latter. The change of sign from positive to negative values around $R/a \sim 0.7$ may reflect the fact that forming a simple Y-shaped junction is rather costly for these smaller R , implying that a different type of

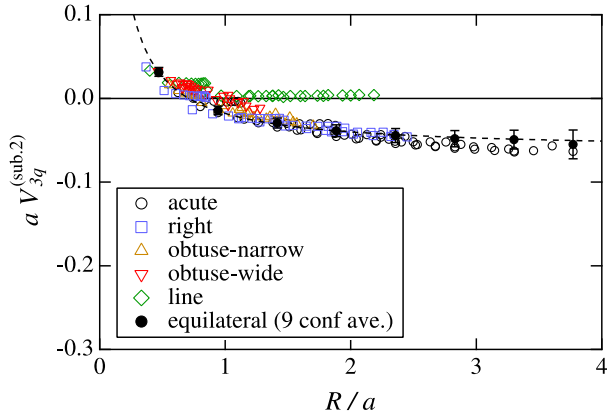


FIG. 18. The same plot as in Fig. 17, but the term $-A_{q\bar{q}}/(2R)$ is further subtracted from the three-quark potential $[V_{3q}^{(\text{sub.2})}$ in Eq. (36)]. The dashed line corresponds to $0.259A_{q\bar{q}}/(2R) + \tilde{\mu}_{3q}$.

flux structure is realized. It would be quite interesting to investigate the energy density of various three-quark systems with the PLCF.

To summarize, the functional form of the three-quark potential for triangle geometries is effectively parametrized by

$$V_{3q} = -\frac{A_{3q}^{(R)}}{R} + \sigma_{q\bar{q}}L_{\text{str}} + \frac{3}{2}\mu_{q\bar{q}} + \tilde{\mu}_{3q}. \quad (37)$$

On the other hand, the functional form for LIN can be described by the half of the sum of the quark-antiquark potential,

$$V_{3q} = \frac{1}{2} \sum_{i=1}^3 V_{q\bar{q}}(r_i), \quad (38)$$

up to the tiny 0.3% relative error as shown in Sec. III D. We cannot answer here whether or not both functional forms can change continuously depending on the movement of quarks, which should be clarified in future study. It is certainly important for this purpose to see the potential of OBTW at long distance in detail. The functional form in Eq. (37) may be similar to that proposed by Takahashi *et al.* [5,6] for triangle geometries, where the potential was parametrized by $V_{3q} = -A_{q\bar{q}}/(2R) + \sigma_{q\bar{q}}Y + \text{constant}$. However, our result shows a noticeable difference from it in terms of the junction term in Eq. (35).

F. Scaling test of the three-quark potential

So far we have concentrated on analyzing the potential at $\beta = 6.00$, and have found the possible functional form of the potential as in Eqs. (37) and (38). We finally examine whether the functional form is still valid even if the lattice spacing decreases or increases. We then computed the three-quark potential at $\beta = 5.85$ and 6.30. We only pay attention to the potential of equilateral triangle geometries

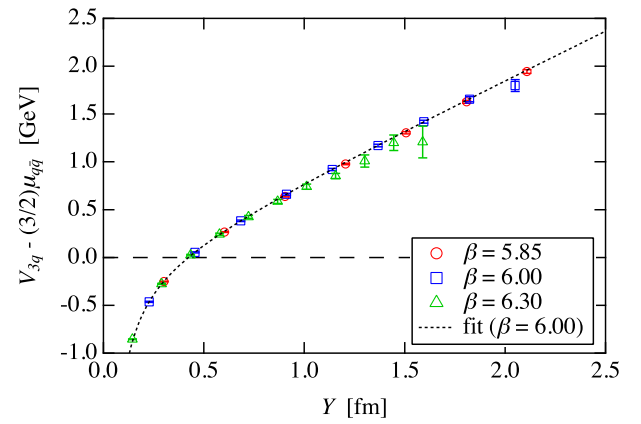


FIG. 19. The three-quark potential as a function of Y in physical unit, where the constant $(3/2)\mu_{q\bar{q}}$ is subtracted. The dotted line corresponds to the fit curve to Eq. (39), which yields $A_{3q}^{(Y)}\hbar c = 0.131(4)$ [GeV/fm], $\sigma_{3q} = 1.02(1)$ [GeV/fm], and $\tilde{\mu}_{3q} = -0.12(2)$ [GeV] with $\chi^2/N_{\text{df}} = 0.02$.

because of the limited computer resources, however, it will provide some hints concerning the scaling behavior of the potential. The number of gauge configurations to compute the final expectation values are not so many, but the statistical errors are highly suppressed by employing the multilevel algorithm with the tuned parameters, where $N_{\text{cnf}} = 8$ at $\beta = 5.85$ with $N_{\text{iupd}} = 500000$, and $N_{\text{cnf}} = 6$ at $\beta = 6.30$ with $N_{\text{iupd}} = 400000$. Typical convergence histories of the PLCF of the equilateral triangle geometry at $\beta = 5.85$ and $\beta = 6.30$ are already shown in Fig. 5.

In Fig. 19, we plot the potential as a function of Y , where physical scales are introduced according to Table I (the raw data and the fit results are summarized in Tables IX and X). In addition, the constant term $(3/2)\mu_{q\bar{q}}a$ is subtracted before we introduce the physical scale for each β value. The constant term $\mu_{q\bar{q}}$ is extracted from the quark-antiquark potential as summarized in Table XII, which reflects the self-energy of a quark and an antiquark, and diverges in the continuum limit $a \rightarrow 0$. We find that the potential beautifully falls into one curve,

$$V_{3q}^{(Y)} = -\frac{A_{3q}^{(Y)}\hbar c}{Y} + \sigma_{3q}Y + \tilde{\mu}_{3q}, \quad (39)$$

indicating a scaling behavior with respect to the lattice spacing.⁵ The quark-antiquark potential used in this analysis also exhibits a good scaling behavior as shown in Fig. 20 (the raw data and the fit results are summarized in Tables XI and XII in Appendix B). Comparison of the

⁵When we put three quarks at $(x, 0, 0)$, $(0, x, 0)$, and $(0, 0, x)$, the distance between the two of three quarks is $r = \sqrt{2}x$ and $Y = \sqrt{6}r = 2\sqrt{3}x$. On the other hand, $R = \sqrt{2}x/3$, and then $R = \sqrt{3}Y/9 = 0.19245Y$. Thus, the function $1/Y$ and $1/R$ is the same for equilateral triangles up to a multiplicative factor.

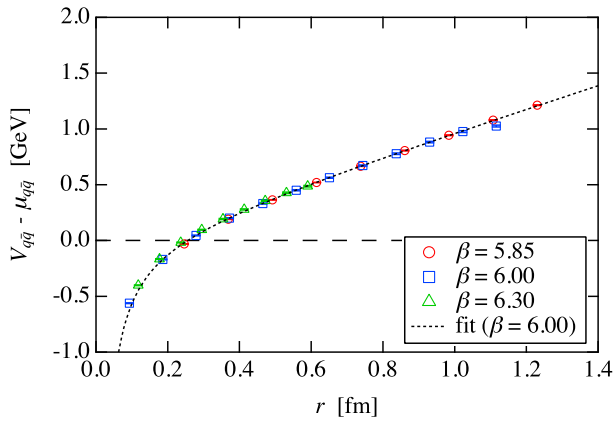


FIG. 20. The quark-antiquark potential as a function of r in physical unit, where the constant $\mu_{q\bar{q}}$ is subtracted. The dotted line is the fit curve to $V_{q\bar{q}}(r) = -A_{q\bar{q}}\hbar c/r + \sigma_{q\bar{q}}r$, which yields $A_{q\bar{q}}\hbar c = 0.0671(6)$ [GeV/fm], $\sigma_{q\bar{q}} = 1.025(4)$ [GeV/fm] with $\chi^2/N_{\text{df}} = 0.013$.

potentials at various β values may be affected by the way of subtraction of the constant μ_{3q} . This uncertainty can however be avoided by looking at the derivative of the potential with respect to Y , which is independent of the constant μ_{3q} . The result is plotted in Fig. 21 and the data fall into a curve given by the derivative of Eq. (39) with respect to Y .

We then look at the scaling behavior of the constant term in the three-quark potential. Although it has already been suggested in Sec. III E that the constant μ_{3q} consists of two contribution $(3/2)\mu_{q\bar{q}}$ and the remnant $\tilde{\mu}_{3q}$,

$$\mu_{3q} = \frac{3}{2}\mu_{q\bar{q}} + \tilde{\mu}_{3q}, \quad (40)$$

we simply compare the behavior of $\mu_{q\bar{q}}/2$ and $\mu_{3q}/3$ in physical unit, which is plotted in Fig. 22 as a function of the

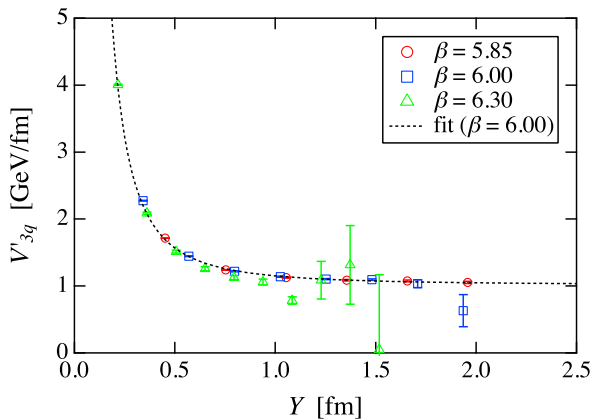


FIG. 21. The derivative of the potential with respect to Y in physical unit. The dotted line corresponds to the fit curve to the derivative of Eq. (39) with respect to Y , which yields $A_{3q}^{(Y)}\hbar c = 0.139(4)$ [GeV/fm], $\sigma = 1.013(7)$ [GeV/fm] with $\chi^2/N_{\text{df}} = 2.0$.

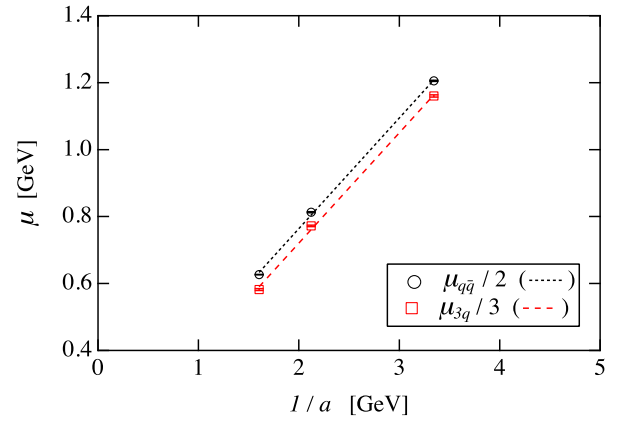


FIG. 22. The scale dependence of the constant term of the quark-antiquark and three-quark potentials per one quark. A naive fit to a linear function yields the slope 0.33 for both cases.

inverse of the lattice spacing $1/a$. If the constant originates only from the divergent self-energies of quarks, both should coincide with each other. As can be seen, the increasing behavior is the same as $1/a$ increases, however, there is a difference by a constant, which seems to be independent of a . Indeed, as we explicitly show in Fig. 23, the remnant of the constant $\tilde{\mu}_{3q}$ seems to exhibit a scaling behavior against a . As already discussed in Sec. III E, $\tilde{\mu}_{3q}$ is absent for LIN and appears only when the three quarks form a triangle. Therefore, it would be quite reasonable to understand that this is caused by the formation of the flux-tube junction, which can reduce the total energy of the three-quark system.

Finally, in Fig. 24, we plot the three-quark potential as a function of R in physical unit after subtracting the confinement and divergent constant terms expected from the quark-antiquark potential, $V_{3q}^{(\text{sub}1)}$ in Eq. (32). The behavior of the potential is nicely described by the functional form in Eq. (33). Although we cannot exclude the possibility of

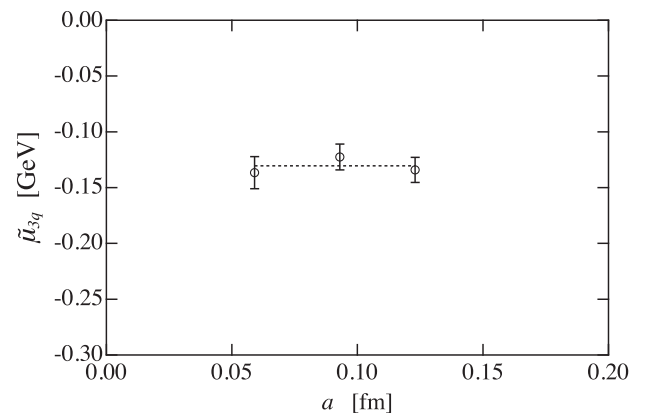


FIG. 23. The scaling behavior of the remnant of the constant term of the three-quark potential $\tilde{\mu}_{3q}$ in Eq. (40). A naive fit to a constant value yields $\tilde{\mu}_{3q} = -0.131(7)$ [GeV].

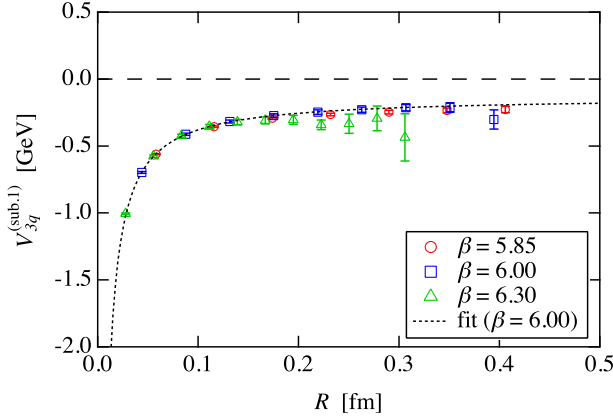


FIG. 24. The three-quark potential as a function of R in physical unit after subtracting the confinement and divergent constant terms expected from the quark-antiquark potential, $V_{3q}^{(\text{sub.1})}$. The dotted line corresponds to the fit curve to $V_{3q}^{(R)} = -A_{3q}^{(R)} \hbar c / R + \tilde{\mu}_{3q}$ in Eq. (33), which yields $A_{3q}^{(R)} \hbar c = 0.0248(5)$ [GeV fm] and $\tilde{\mu}_{3q} = -0.132(8)$ [GeV] with $\chi^2/N_{\text{df}} = 0.04$.

other parametrizations with different distances, such as Y , which is different from R only by a multiplicative factor for the equilateral triangle geometries, this plot and the detailed analysis of the potential at $\beta = 6.00$ in Fig. 17 indicate that the parametrization with R also works well for other three-quark geometries at $\beta = 5.85$ and 6.30 .

IV. SUMMARY

We have investigated the static interquark potential for the three-quark system, the three-quark potential, in SU(3) lattice gauge theory at zero temperature by using Monte Carlo simulations. The crucial difference of our study from earlier ones by other groups is that we have used the Polyakov loop correlation function (PLCF) composed of the three Polyakov loops as the three-quark source instead of the three-quark Wilson loop, and thus, our results are not contaminated by systematic effects due to the spatial Wilson lines. By employing the multilevel algorithm extensively, we have then obtained remarkably accurate data on the potential for $O(200)$ sets of the three-quark geometries, which include not only the cases that three quarks are put at the vertices of acute (ACT), right (RGT), and obtuse (OBTN and OBTW) triangles, but also the extreme cases such that three quarks are put in line (LIN). As a special case, we have also investigated the quark-diquark (QDQ) potential.

What we have shown on the three-quark potential is summarized as follows.

- (i) The potentials of ACT, RGT, OBTN with $r_{\text{min}}/a > 2$ plotted against L_{str} can fall into one curve, which

show the same linearly-rising behavior at long distance as in the quark-antiquark potential.

- (ii) The potential of QDQ is identical to the quark-antiquark potential as in Eq. (26) except for the constant shift.
- (iii) The string tension of the potential, identified as the coefficient in front of L_{str} , is common to that of the quark-antiquark potential (we have shown this without a fit procedure).
- (iv) The potentials of triangle geometries are clearly different from the half of the sum of the two-body quark-antiquark potential when the size of the triangle becomes larger, which can be described by the functional form in Eq. (37).
- (v) The potential of LIN is very close to the half of the sum of the two-body quark-antiquark potentials, which can be described by the functional form in Eq. (38) (up to a tiny relative error about 0.3% at $\beta = 6.00$).
- (vi) The potential, its derivative, and the remnant of the constant term, which we call the junction term, show good scaling behaviors with respect to the lattice spacing (although only the equilateral triangle geometries have been examined).

It seems that there is no unique functional form of the potential which covers all three-quark geometries, which in turn implies that the potential is very sensitive not only to the location of three quarks but also to the nontrivial flux-tube structure spanned among the three quarks. The functional forms that we have successfully categorized into three types as in Eqs. (26), (37), and (38) clearly indicate this feature. Probably, the potential of OBTW, which has not been addressed fully in the present study, may play an intermediate role between ACT-RGT-OBTN and LIN. It must be quite important to look at the distribution of energy density in the three-quark system at zero temperature by using the PLCF as in the finite temperature case [13,38,39].

In order to apply the three-quark potential to baryon spectroscopy, on the other hand, it would be desirable to have a unique functional form. This may be possible by introducing a kind of a form factor. One of the practical ideas may be to extend the functional form that we have found further by using the distance such as h , an averaged distance between the Fermat-Torricelli point and three sides of a triangle. As we have demonstrated in Fig. 16, the difference between all three-quark potentials from the half of the sum of the quark-antiquark potential can be described by a quadratic function of h .

ACKNOWLEDGMENTS

Y.K. was partially supported by the Ministry of Education, Science, Sports and Culture, Japan, Grant-in-Aid for Young Scientists (B) (24740176). Our numerical simulations were performed on supercomputers NEC SX8

at Research Center for Nuclear Physics (RCNP), and NEC SX-ACE at Cybermedia Center (CMC), Osaka University. We thank V. Dmitrašinović, N. Brambilla, Ph. de Forcrand, and the anonymous referee of Physical Review D for useful comments on the manuscript.

APPENDIX A: THE THREE-QUARK POTENTIAL DATA

TABLE III. List of the three-quark potential (ACT).

No.	\vec{x}_1	\vec{x}_2	\vec{x}_3	r_1	r_2	r_3	θ_{\max}	V_{3q}
1	(1,0,0)	(0,1,0)	(0,0,1)	1.41	1.41	1.41	60	0.9300
2	(2,0,0)	(0,2,0)	(0,0,2)	2.83	2.83	2.83	60	1.1723
3	(3,0,0)	(0,3,0)	(0,0,3)	4.24	4.24	4.24	60	1.3252
4	(4,0,0)	(0,4,0)	(0,0,4)	5.66	5.66	5.66	60	1.4538
5	(5,0,0)	(0,5,0)	(0,0,5)	7.07	7.07	7.07	60	1.5737
6	(6,0,0)	(0,6,0)	(0,0,6)	8.49	8.49	8.49	60	1.6899
7	(7,0,0)	(0,7,0)	(0,0,7)	9.90	9.90	9.90	60	1.8050
8	(8,0,0)	(0,8,0)	(0,0,8)	11.31	11.31	11.31	60	1.9210
9	(2,0,0)	(0,1,0)	(0,0,1)	1.41	2.24	2.24	72	1.0347
10	(3,0,0)	(0,1,0)	(0,0,1)	1.41	3.16	3.16	77	1.1156
11	(4,0,0)	(0,1,0)	(0,0,1)	1.41	4.12	4.12	80	1.1822
12	(5,0,0)	(0,1,0)	(0,0,1)	1.41	5.10	5.10	82	1.2412
13	(6,0,0)	(0,1,0)	(0,0,1)	1.41	6.08	6.08	83	1.2959
14	(7,0,0)	(0,1,0)	(0,0,1)	1.41	7.07	7.07	84	1.3481
15	(8,0,0)	(0,1,0)	(0,0,1)	1.41	8.06	8.06	85	1.3988
16	(9,0,0)	(0,1,0)	(0,0,1)	1.41	9.06	9.06	86	1.4483
17	(10,0,0)	(0,1,0)	(0,0,1)	1.41	10.05	10.05	86	1.4972
18	(11,0,0)	(0,1,0)	(0,0,1)	1.41	11.05	11.05	86	1.5430
19	(1,0,0)	(0,2,0)	(0,0,2)	2.83	2.24	2.24	78	1.1155
20	(3,0,0)	(0,2,0)	(0,0,2)	2.83	3.61	3.61	67	1.2310
21	(4,0,0)	(0,2,0)	(0,0,2)	2.83	4.47	4.47	72	1.2873
22	(5,0,0)	(0,2,0)	(0,0,2)	2.83	5.39	5.39	75	1.3410
23	(6,0,0)	(0,2,0)	(0,0,2)	2.83	6.32	6.32	77	1.3927
24	(7,0,0)	(0,2,0)	(0,0,2)	2.83	7.28	7.28	79	1.4432
25	(8,0,0)	(0,2,0)	(0,0,2)	2.83	8.25	8.25	80	1.4926
26	(9,0,0)	(0,2,0)	(0,0,2)	2.83	9.22	9.22	81	1.5414
27	(10,0,0)	(0,2,0)	(0,0,2)	2.83	10.20	10.20	82	1.5897
28	(11,0,0)	(0,2,0)	(0,0,2)	2.83	11.18	11.18	83	1.6348
29	(1,0,0)	(0,3,0)	(0,0,3)	4.24	3.16	3.16	84	1.2476
30	(2,0,0)	(0,3,0)	(0,0,3)	4.24	3.61	3.61	72	1.2820
31	(4,0,0)	(0,3,0)	(0,0,3)	4.24	5.00	5.00	65	1.3718
32	(5,0,0)	(0,3,0)	(0,0,3)	4.24	5.83	5.83	69	1.4196
33	(6,0,0)	(0,3,0)	(0,0,3)	4.24	6.71	6.71	72	1.4676
34	(7,0,0)	(0,3,0)	(0,0,3)	4.24	7.62	7.62	74	1.5154
35	(8,0,0)	(0,3,0)	(0,0,3)	4.24	8.54	8.54	76	1.5632
36	(9,0,0)	(0,3,0)	(0,0,3)	4.24	9.49	9.49	77	1.6107
37	(10,0,0)	(0,3,0)	(0,0,3)	4.24	10.44	10.44	78	1.6579
38	(11,0,0)	(0,3,0)	(0,0,3)	4.24	11.40	11.40	79	1.7022
39	(1,0,0)	(0,4,0)	(0,0,4)	5.66	4.12	4.12	87	1.3578
40	(2,0,0)	(0,4,0)	(0,0,4)	5.66	4.47	4.47	78	1.3814
41	(3,0,0)	(0,4,0)	(0,0,4)	5.66	5.00	5.00	69	1.4148
42	(5,0,0)	(0,4,0)	(0,0,4)	5.66	6.40	6.40	64	1.4961

(Table continued)

TABLE III. (Continued)

No.	\vec{x}_1	\vec{x}_2	\vec{x}_3	r_1	r_2	r_3	θ_{\max}	V_{3q}
43	(6,0,0)	(0,4,0)	(0,0,4)	5.66	7.21	7.21	67	1.5401
44	(7,0,0)	(0,4,0)	(0,0,4)	5.66	8.06	8.06	69	1.5852
45	(8,0,0)	(0,4,0)	(0,0,4)	5.66	8.94	8.94	72	1.6307
46	(9,0,0)	(0,4,0)	(0,0,4)	5.66	9.85	9.85	73	1.6768
47	(10,0,0)	(0,4,0)	(0,0,4)	5.66	10.77	10.77	75	1.7225
48	(11,0,0)	(0,4,0)	(0,0,4)	5.66	11.70	11.70	76	1.7655
49	(1,0,0)	(0,5,0)	(0,0,5)	7.07	5.10	5.10	88	1.4579
50	(2,0,0)	(0,5,0)	(0,0,5)	7.07	5.39	5.39	82	1.4758
51	(3,0,0)	(0,5,0)	(0,0,5)	7.07	5.83	5.83	75	1.5028
52	(4,0,0)	(0,5,0)	(0,0,5)	7.07	6.40	6.40	67	1.5361
53	(6,0,0)	(0,5,0)	(0,0,5)	7.07	7.81	7.81	63	1.6140
54	(7,0,0)	(0,5,0)	(0,0,5)	7.07	8.60	8.60	66	1.6563
55	(8,0,0)	(0,5,0)	(0,0,5)	7.07	9.43	9.43	68	1.6994
56	(9,0,0)	(0,5,0)	(0,0,5)	7.07	10.30	10.30	70	1.7439
57	(10,0,0)	(0,5,0)	(0,0,5)	7.07	11.18	11.18	72	1.7877
58	(11,0,0)	(0,5,0)	(0,0,5)	7.07	12.08	12.08	73	1.8307
59	(1,0,0)	(0,6,0)	(0,0,6)	8.49	6.08	6.08	88	1.5530
60	(2,0,0)	(0,6,0)	(0,0,6)	8.49	6.32	6.32	84	1.5676
61	(3,0,0)	(0,6,0)	(0,0,6)	8.49	6.71	6.71	78	1.5902
62	(4,0,0)	(0,6,0)	(0,0,6)	8.49	7.21	7.21	72	1.6191
63	(5,0,0)	(0,6,0)	(0,0,6)	8.49	7.81	7.81	66	1.6529
64	(7,0,0)	(0,6,0)	(0,0,6)	8.49	9.22	9.22	63	1.7295
65	(8,0,0)	(0,6,0)	(0,0,6)	8.49	10.00	10.00	65	1.7699
66	(9,0,0)	(0,6,0)	(0,0,6)	8.49	10.82	10.82	67	1.8108
67	(10,0,0)	(0,6,0)	(0,0,6)	8.49	11.66	11.66	69	1.8556
68	(11,0,0)	(0,6,0)	(0,0,6)	8.49	12.53	12.53	70	1.9051

TABLE IV. List of the three-quark potential (RGT).

No.	\vec{x}_1	\vec{x}_2	\vec{x}_3	r_1	r_2	r_3	θ_{\max}	V_{3q}
1	(1,0,0)	(0,1,0)	(0,0,0)	1.00	1.00	1.41	90	0.8139
2	(2,0,0)	(0,1,0)	(0,0,0)	1.00	2.00	2.24	90	0.9588
3	(3,0,0)	(0,1,0)	(0,0,0)	1.00	3.00	3.16	90	1.0500
4	(4,0,0)	(0,1,0)	(0,0,0)	1.00	4.00	4.12	90	1.1197
5	(5,0,0)	(0,1,0)	(0,0,0)	1.00	5.00	5.10	90	1.1799
6	(6,0,0)	(0,1,0)	(0,0,0)	1.00	6.00	6.08	90	1.2352
7	(2,0,0)	(0,2,0)	(0,0,0)	2.00	2.00	2.83	90	1.0796
8	(3,0,0)	(0,2,0)	(0,0,0)	2.00	3.00	3.61	90	1.1597
9	(4,0,0)	(0,2,0)	(0,0,0)	2.00	4.00	4.47	90	1.2244
10	(5,0,0)	(0,2,0)	(0,0,0)	2.00	5.00	5.39	90	1.2820
11	(7,0,0)	(0,1,0)	(0,0,0)	1.00	7.00	7.07	90	1.2877
12	(8,0,0)	(0,1,0)	(0,0,0)	1.00	8.00	8.06	90	1.3386
13	(9,0,0)	(0,1,0)	(0,0,0)	1.00	9.00	9.06	90	1.3884
14	(10,0,0)	(0,1,0)	(0,0,0)	1.00	10.00	10.05	90	1.4373
15	(11,0,0)	(0,1,0)	(0,0,0)	1.00	11.00	11.05	90	1.4831
16	(6,0,0)	(0,2,0)	(0,0,0)	2.00	6.00	6.32	90	1.3359
17	(7,0,0)	(0,2,0)	(0,0,0)	2.00	7.00	7.28	90	1.3875
18	(8,0,0)	(0,2,0)	(0,0,0)	2.00	8.00	8.25	90	1.4377
19	(9,0,0)	(0,2,0)	(0,0,0)	2.00	9.00	9.22	90	1.4872
20	(10,0,0)	(0,2,0)	(0,0,0)	2.00	10.00	10.20	90	1.5358

(Table continued)

TABLE IV. (Continued)

No.	\vec{x}_1	\vec{x}_2	\vec{x}_3	r_1	r_2	r_3	θ_{\max}	V_{3q}
21	(11,0,0)	(0,2,0)	(0,0,0)	2.00	11.00	11.18	90	1.5813
22	(3,0,0)	(0,3,0)	(0,0,0)	3.00	3.00	4.24	90	1.2322
23	(4,0,0)	(0,3,0)	(0,0,0)	3.00	4.00	5.00	90	1.2922
24	(5,0,0)	(0,3,0)	(0,0,0)	3.00	5.00	5.83	90	1.3470
25	(6,0,0)	(0,3,0)	(0,0,0)	3.00	6.00	6.71	90	1.3990
26	(7,0,0)	(0,3,0)	(0,0,0)	3.00	7.00	7.62	90	1.4495
27	(8,0,0)	(0,3,0)	(0,0,0)	3.00	8.00	8.54	90	1.4990
28	(9,0,0)	(0,3,0)	(0,0,0)	3.00	9.00	9.49	90	1.5478
29	(10,0,0)	(0,3,0)	(0,0,0)	3.00	10.00	10.44	90	1.5960
30	(11,0,0)	(0,3,0)	(0,0,0)	3.00	11.00	11.40	90	1.6412
31	(4,0,0)	(0,4,0)	(0,0,0)	4.00	4.00	5.66	90	1.3487
32	(5,0,0)	(0,4,0)	(0,0,0)	4.00	5.00	6.40	90	1.4010
33	(6,0,0)	(0,4,0)	(0,0,0)	4.00	6.00	7.21	90	1.4513
34	(7,0,0)	(0,4,0)	(0,0,0)	4.00	7.00	8.06	90	1.5005
35	(8,0,0)	(0,4,0)	(0,0,0)	4.00	8.00	8.94	90	1.5489
36	(9,0,0)	(0,4,0)	(0,0,0)	4.00	9.00	9.85	90	1.5972
37	(10,0,0)	(0,4,0)	(0,0,0)	4.00	10.00	10.77	90	1.6451
38	(11,0,0)	(0,4,0)	(0,0,0)	4.00	11.00	11.70	90	1.6896
39	(5,0,0)	(0,5,0)	(0,0,0)	5.00	5.00	7.07	90	1.4513
40	(6,0,0)	(0,5,0)	(0,0,0)	5.00	6.00	7.81	90	1.5001
41	(7,0,0)	(0,5,0)	(0,0,0)	5.00	7.00	8.60	90	1.5481
42	(8,0,0)	(0,5,0)	(0,0,0)	5.00	8.00	9.43	90	1.5958
43	(9,0,0)	(0,5,0)	(0,0,0)	5.00	9.00	10.30	90	1.6433

TABLE V. List of the three-quark potential (OBTN).

No.	\vec{x}_1	\vec{x}_2	\vec{x}_3	r_1	r_2	r_3	θ_{\max}	V_{3q}
1	(2,0,0)	(1,0,0)	(0,0,2)	2.24	2.83	1.00	117	1.0049
2	(3,0,0)	(1,0,0)	(0,0,2)	2.24	3.61	2.00	117	1.1264
3	(4,0,0)	(1,0,0)	(0,0,2)	2.24	4.47	3.00	117	1.2051
4	(5,0,0)	(1,0,0)	(0,0,2)	2.24	5.39	4.00	117	1.2684
5	(2,0,0)	(1,0,0)	(0,0,3)	3.16	3.61	1.00	108	1.0742
6	(3,0,0)	(1,0,0)	(0,0,3)	3.16	4.24	2.00	108	1.1881
7	(4,0,0)	(1,0,0)	(0,0,3)	3.16	5.00	3.00	108	1.2621
8	(5,0,0)	(1,0,0)	(0,0,3)	3.16	5.83	4.00	108	1.3225
9	(2,0,0)	(1,0,0)	(0,0,4)	4.12	4.47	1.00	104	1.1352
10	(3,0,0)	(1,0,0)	(0,0,4)	4.12	5.00	2.00	104	1.2443
11	(3,0,0)	(2,0,0)	(0,0,4)	4.47	5.00	1.00	117	1.1621
12	(4,0,0)	(1,0,0)	(0,0,4)	4.12	5.66	3.00	104	1.3147
13	(4,0,0)	(2,0,0)	(0,0,4)	4.47	5.66	2.00	117	1.2738
14	(5,0,0)	(1,0,0)	(0,0,4)	4.12	6.40	4.00	104	1.3726
15	(5,0,0)	(2,0,0)	(0,0,4)	4.47	6.40	3.00	117	1.3457
16	(2,0,0)	(1,0,0)	(0,0,5)	5.10	5.39	1.00	101	1.1910
17	(3,0,0)	(1,0,0)	(0,0,5)	5.10	5.83	2.00	101	1.2971
18	(3,0,0)	(2,0,0)	(0,0,5)	5.39	5.83	1.00	112	1.2117
19	(4,0,0)	(1,0,0)	(0,0,5)	5.10	6.40	3.00	101	1.3649
20	(4,0,0)	(2,0,0)	(0,0,5)	5.39	6.40	2.00	112	1.3206
21	(5,0,0)	(1,0,0)	(0,0,5)	5.10	7.07	4.00	101	1.4207
22	(5,0,0)	(2,0,0)	(0,0,5)	5.39	7.07	3.00	112	1.3904
23	(2,0,0)	(1,0,0)	(0,0,6)	6.08	6.32	1.00	99	1.2438
24	(3,0,0)	(1,0,0)	(0,0,6)	6.08	6.71	2.00	99	1.3479
25	(3,0,0)	(2,0,0)	(0,0,6)	6.32	6.71	1.00	108	1.2604
26	(4,0,0)	(1,0,0)	(0,0,6)	6.08	7.21	3.00	99	1.4139
27	(4,0,0)	(2,0,0)	(0,0,6)	6.32	7.21	2.00	108	1.3674

TABLE VI. List of the three-quark potential (OBTW).

No.	\vec{x}_1	\vec{x}_2	\vec{x}_3	r_1	r_2	r_3	θ_{\max}	V_{3q}
1	(2,0,0)	(1,0,0)	(0,0,1)	1.41	2.24	1.00	135	0.9243
2	(3,0,0)	(1,0,0)	(0,0,1)	1.41	3.16	2.00	135	1.0570
3	(3,0,0)	(2,0,0)	(0,0,1)	2.24	3.16	1.00	153	1.0169
4	(4,0,0)	(1,0,0)	(0,0,1)	1.41	4.12	3.00	135	1.1410
5	(4,0,0)	(2,0,0)	(0,0,1)	2.24	4.12	2.00	153	1.1425
6	(4,0,0)	(3,0,0)	(0,0,1)	3.16	4.12	1.00	162	1.0904
7	(5,0,0)	(1,0,0)	(0,0,1)	1.41	5.10	4.00	135	1.2068
8	(5,0,0)	(2,0,0)	(0,0,1)	2.24	5.10	3.00	153	1.2226
9	(5,0,0)	(3,0,0)	(0,0,1)	3.16	5.10	2.00	162	1.2122
10	(5,0,0)	(4,0,0)	(0,0,1)	4.12	5.10	1.00	166	1.1529
11	(3,0,0)	(2,0,0)	(0,0,2)	2.83	3.61	1.00	135	1.0618
12	(4,0,0)	(2,0,0)	(0,0,2)	2.83	4.47	2.00	135	1.1821
13	(4,0,0)	(3,0,0)	(0,0,2)	3.61	4.47	1.00	146	1.1184
14	(5,0,0)	(2,0,0)	(0,0,2)	2.83	5.39	3.00	135	1.2596
15	(5,0,0)	(3,0,0)	(0,0,2)	3.61	5.39	2.00	146	1.2374
16	(5,0,0)	(4,0,0)	(0,0,2)	4.47	5.39	1.00	153	1.1725
17	(3,0,0)	(2,0,0)	(0,0,3)	3.61	4.24	1.00	124	1.1117
18	(4,0,0)	(2,0,0)	(0,0,3)	3.61	5.00	2.00	124	1.2272
19	(4,0,0)	(3,0,0)	(0,0,3)	4.24	5.00	1.00	135	1.1551
20	(5,0,0)	(2,0,0)	(0,0,3)	3.61	5.83	3.00	124	1.3017
21	(5,0,0)	(3,0,0)	(0,0,3)	4.24	5.83	2.00	135	1.2711
22	(5,0,0)	(4,0,0)	(0,0,3)	5.00	5.83	1.00	143	1.2007
23	(4,0,0)	(3,0,0)	(0,0,4)	5.00	5.66	1.00	127	1.1962
24	(5,0,0)	(3,0,0)	(0,0,4)	5.00	6.40	2.00	127	1.3094
25	(5,0,0)	(4,0,0)	(0,0,4)	5.66	6.40	1.00	135	1.2346
26	(4,0,0)	(3,0,0)	(0,0,5)	5.83	6.40	1.00	121	1.2394
27	(5,0,0)	(3,0,0)	(0,0,5)	5.83	7.07	2.00	121	1.3503
28	(5,0,0)	(4,0,0)	(0,0,5)	6.40	7.07	1.00	129	1.2721

TABLE VII. List of the three-quark potential (LIN).

No.	\vec{x}_1	\vec{x}_2	\vec{x}_3	r_1	r_2	r_3	θ_{\max}	V_{3q}
1	(2,0,0)	(1,0,0)	(0,0,0)	1.00	2.00	1.00	180	0.8478
2	(3,0,0)	(1,0,0)	(0,0,0)	1.00	3.00	2.00	180	0.9914
3	(4,0,0)	(1,0,0)	(0,0,0)	1.00	4.00	3.00	180	1.0786
4	(4,0,0)	(2,0,0)	(0,0,0)	2.00	4.00	2.00	180	1.1203
5	(5,0,0)	(1,0,0)	(0,0,0)	1.00	5.00	4.00	180	1.1457
6	(5,0,0)	(2,0,0)	(0,0,0)	2.00	5.00	3.00	180	1.2017
7	(6,0,0)	(1,0,0)	(0,0,0)	1.00	6.00	5.00	180	1.2044
8	(6,0,0)	(2,0,0)	(0,0,0)	2.00	6.00	4.00	180	1.2661
9	(6,0,0)	(3,0,0)	(0,0,0)	3.00	6.00	3.00	180	1.2803
10	(7,0,0)	(1,0,0)	(0,0,0)	1.00	7.00	6.00	180	1.2588
11	(7,0,0)	(2,0,0)	(0,0,0)	2.00	7.00	5.00	180	1.3233
12	(7,0,0)	(3,0,0)	(0,0,0)	3.00	7.00	4.00	180	1.3434
13	(8,0,0)	(1,0,0)	(0,0,0)	1.00	8.00	7.00	180	1.3108
14	(8,0,0)	(2,0,0)	(0,0,0)	2.00	8.00	6.00	180	1.3769
15	(8,0,0)	(3,0,0)	(0,0,0)	3.00	8.00	5.00	180	1.3998
16	(8,0,0)	(4,0,0)	(0,0,0)	4.00	8.00	4.00	180	1.4055
17	(9,0,0)	(1,0,0)	(0,0,0)	1.00	9.00	8.00	180	1.3612
18	(9,0,0)	(2,0,0)	(0,0,0)	2.00	9.00	7.00	180	1.4283
19	(9,0,0)	(3,0,0)	(0,0,0)	3.00	9.00	6.00	180	1.4527
20	(9,0,0)	(4,0,0)	(0,0,0)	4.00	9.00	5.00	180	1.4614
21	(10,0,0)	(1,0,0)	(0,0,0)	1.00	10.00	9.00	180	1.4108

(Table continued)

TABLE VII. (*Continued*)

No.	\vec{x}_1	\vec{x}_2	\vec{x}_3	r_1	r_2	r_3	θ_{\max}	V_{3q}
22	(10,0,0)	(2,0,0)	(0,0,0)	2.00	10.00	8.00	180	1.4786
23	(10,0,0)	(3,0,0)	(0,0,0)	3.00	10.00	7.00	180	1.5040
24	(10,0,0)	(4,0,0)	(0,0,0)	4.00	10.00	6.00	180	1.5142
25	(10,0,0)	(5,0,0)	(0,0,0)	5.00	10.00	5.00	180	1.5171
26	(11,0,0)	(1,0,0)	(0,0,0)	1.00	11.00	10.00	180	1.4591
27	(11,0,0)	(2,0,0)	(0,0,0)	2.00	11.00	9.00	180	1.5279
28	(11,0,0)	(3,0,0)	(0,0,0)	3.00	11.00	8.00	180	1.5540
29	(11,0,0)	(4,0,0)	(0,0,0)	4.00	11.00	7.00	180	1.5654
30	(11,0,0)	(5,0,0)	(0,0,0)	5.00	11.00	6.00	180	1.5697
31	(12,0,0)	(1,0,0)	(0,0,0)	1.00	12.00	11.00	180	1.4987
32	(12,0,0)	(2,0,0)	(0,0,0)	2.00	12.00	10.00	180	1.5740

TABLE VIII. List of the three-quark potential (QDQ).

No.	\vec{x}_1	\vec{x}_2	\vec{x}_3	r_1	r_2	r_3	θ_{\max}	V_{3q}
1	(1,0,0)	(0,0,0)	(0,0,0)	0.00	1.00	1.00	—	0.5480
2	(2,0,0)	(0,0,0)	(0,0,0)	0.00	2.00	2.00	—	0.7331
3	(3,0,0)	(0,0,0)	(0,0,0)	0.00	3.00	3.00	—	0.8347
4	(4,0,0)	(0,0,0)	(0,0,0)	0.00	4.00	4.00	—	0.9075
5	(5,0,0)	(0,0,0)	(0,0,0)	0.00	5.00	5.00	—	0.9689
6	(6,0,0)	(0,0,0)	(0,0,0)	0.00	6.00	6.00	—	1.0248
7	(7,0,0)	(0,0,0)	(0,0,0)	0.00	7.00	7.00	—	1.0777
8	(8,0,0)	(0,0,0)	(0,0,0)	0.00	8.00	8.00	—	1.1287
9	(9,0,0)	(0,0,0)	(0,0,0)	0.00	9.00	9.00	—	1.1786
10	(10,0,0)	(0,0,0)	(0,0,0)	0.00	10.00	10.00	—	1.2277
11	(11,0,0)	(0,0,0)	(0,0,0)	0.00	11.00	11.00	—	1.2736
12	(12,0,0)	(0,0,0)	(0,0,0)	0.00	12.00	12.00	—	1.2979
13	(1,0,0)	(1,0,0)	(0,0,1)	1.41	1.41	0.00	—	0.6650
14	(2,0,0)	(2,0,0)	(0,0,1)	2.24	2.24	0.00	—	0.7693
15	(3,0,0)	(3,0,0)	(0,0,1)	3.16	3.16	0.00	—	0.8498
16	(4,0,0)	(4,0,0)	(0,0,1)	4.12	4.12	0.00	—	0.9161
17	(5,0,0)	(5,0,0)	(0,0,1)	5.10	5.10	0.00	—	0.9748
18	(1,0,0)	(1,0,0)	(0,0,2)	2.24	2.24	0.00	—	0.7693
19	(2,0,0)	(2,0,0)	(0,0,2)	2.83	2.83	0.00	—	0.8255
20	(3,0,0)	(3,0,0)	(0,0,2)	3.61	3.61	0.00	—	0.8832
21	(4,0,0)	(4,0,0)	(0,0,2)	4.47	4.47	0.00	—	0.9385
22	(5,0,0)	(5,0,0)	(0,0,2)	5.39	5.39	0.00	—	0.9914
23	(1,0,0)	(1,0,0)	(0,0,3)	3.16	3.16	0.00	—	0.8498

TABLE IX. The three-quark potentials of the equilateral geometries at $\beta = 5.85$ ($N_{\text{iupd}} = 500000$ and $N_{\text{cnf}} = 8$), 6.00 ($N_{\text{iupd}} = 500000$ and $N_{\text{cnf}} = 9$), and 6.30 ($N_{\text{iupd}} = 400000$ and $N_{\text{cnf}} = 6$), where the three quarks are placed at $(x, 0, 0)$, $(0, x, 0)$ and $(0, 0, x)$. The distances $Y = \sqrt{6}x$ and $R = \sqrt{3}Y/9 = \sqrt{2}x/3$ are used when we plot the potential data. The corresponding plot is shown in Fig. 19.

x/a	Y/a	R/a	$\beta = 5.85$	$\beta = 6.00$	$\beta = 6.30$
1	2.449	0.471	1.01563(39)	0.93078(23)	0.82543(12)
2	4.899	0.943	1.3374(11)	1.17491(76)	0.99852(53)
3	7.348	1.414	1.5703(21)	1.3300(15)	1.0886(12)
4	9.798	1.886	1.7813(34)	1.4609(23)	1.1540(22)

(Table continued)

TABLE IX. (*Continued*)

x/a	Y/a	R/a	$\beta = 5.85$	$\beta = 6.00$	$\beta = 6.30$
5	12.247	2.357	1.9855(53)	1.5830(33)	1.2083(36)
6	14.697	2.828	2.1871(78)	1.7013(42)	1.2569(48)
7	17.146	3.300	2.385(10)	1.8187(52)	1.3026(66)
8	19.596	3.771		1.930(11)	1.3364(70)
9	22.045	4.243		1.997(27)	1.383(18)
10	24.495	4.714			1.440(23)
11	26.944	5.185			1.442(48)

TABLE X. Fit results of the three-quark potential in Table IX to $V_{3q}^{(Y)} = -A_{3q}^{(Y)}/Y + \sigma_{3q}Y + \mu_{3q}$.

β	$A_{3q}^{(Y)}$	$\sigma_{3q}a^2$	$\mu_{3q}a$	fit range x/a (Y/a)	χ^2/N_{df}
5.85	0.64(1)	0.0776(5)	1.089(5)	1–7 (2.45–17.1)	0.15
6.00	0.662(6)	0.0446(3)	1.092(3)	1–8 (2.45–19.6)	0.09
6.30	0.635(6)	0.0180(3)	1.041(3)	1–7 (2.45–17.1)	2.1

APPENDIX B: THE QUARK-ANTIQUARK POTENTIAL DATA

TABLE XI. The quark-antiquark potentials at $\beta = 5.85$ ($N_{\text{iupd}} = 50000$ and $N_{\text{cnf}} = 133$), 6.00 ($N_{\text{iupd}} = 100000$ and $N_{\text{cnf}} = 20$), and 6.30 ($N_{\text{iupd}} = 6000$ and $N_{\text{cnf}} = 40$), where the quark and antiquark are separated only along the on-axis. For other simulation parameters, see Table I. The data at $\beta = 5.85$ and 6.30 were computed when we studied the relativistic corrections to the quark-antiquark potential [32,33] and for this reason some parts remain blank, which however are harmless in the present analysis. The corresponding plot is shown in Fig. 20.

r/a	$\beta = 5.85$	$\beta = 6.00$	$\beta = 6.30$
1		0.501511(36)	
2	0.762272(85)	0.68631(12)	0.600853(55)
3	0.90051(16)	0.78796(24)	0.67114(11)
4	1.00877(25)	0.86105(39)	0.71569(19)
5	1.10516(35)	0.92273(56)	0.74970(30)
6	1.19592(46)	0.97891(75)	0.77837(41)
7	1.28359(58)	1.03203(97)	0.80403(56)
8	1.36941(71)	1.0833(12)	0.82733(74)
9	1.45401(84)	1.1333(14)	0.84850(96)
10	1.53776(99)	1.1820(17)	0.8667(12)
11		1.2269(21)	
12		1.2499(24)	

TABLE XII. Fit results of the quark-antiquark potential in Table XI to $V_{q\bar{q}}(r) = -A_{q\bar{q}}/r + \sigma_{q\bar{q}}r + \mu_{q\bar{q}}$.

β	$A_{q\bar{q}}$	$\sigma_{q\bar{q}}a^2$	$\mu_{q\bar{q}}a$	fit range r/a	χ^2/N_{df}
5.85	0.354(2)	0.0790(1)	0.781(1)	3–10	1.1
6.00	0.340(2)	0.0449(2)	0.766(1)	2–10	0.13
6.30	0.313(2)	0.0182(1)	0.721(1)	3–10	1.2

TABLE XIII. The quark-antiquark potential at $\beta=6.00$ ($N_{\text{upd}} = 100000$ and $N_{\text{cnf}} = 20$), where the quark and antiquark are separated along the off-axis. For other simulation parameters, see Table I. The Euclidean distance for the label (i, j, k) is $r/a = \sqrt{i^2 + j^2 + k^2}$. These data are used when comparing the three-quark potential with the quark-antiquark potential at $\beta = 6.00$. All data including the on-axis data at $\beta = 6.00$ in Table XI are plotted in Fig. 25.

i	$(i, i, 0)$	(i, i, i)	$(2i, i, 0)$
1	0.618206(71)	0.67289(10)	0.72246(15)
2	0.77882(23)	0.82851(33)	0.89243(48)
3	0.87886(45)	0.93620(65)	1.01763(94)
4	0.96147(74)	1.0301(10)	1.1316(15)
5	1.0370(11)	1.1185(15)	1.2404(23)
6	1.1091(15)	1.2040(20)	1.3173(30)
7	1.1792(20)	1.2879(27)	
8	1.2480(26)	1.3705(36)	
9	1.3155(33)	1.4518(55)	
10	1.3797(45)	1.521(10)	
11	1.4311(70)	1.565(27)	
12	1.4500(89)	1.567(31)	

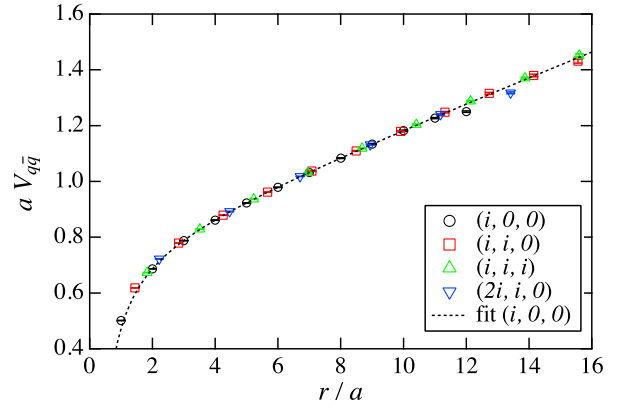


FIG. 25. The quark-antiquark potential at $\beta = 6.00$ as a function of the interquark distance r/a . The raw data and the fit results are summarized in Tables XI, XII, and XIII.

-
- [1] R. Sommer and J. Wosiek, Baryonic loops and the confinement in the three quark channel, *Phys. Lett.* **149B**, 497 (1984).
- [2] R. Sommer and J. Wosiek, Baryonic strings on a lattice, *Nucl. Phys.* **B267**, 531 (1986).
- [3] H. Thacker, E. Eichten, and J. Sexton, The three-body potential for heavy quark baryons in lattice QCD, *Nucl. Phys. B, Proc. Suppl.* **4**, 234 (1988).
- [4] G. S. Bali, QCD forces and heavy quark bound states, *Phys. Rep.* **343**, 1 (2001).
- [5] T. T. Takahashi, H. Matsufuru, Y. Nemoto, and H. Suganuma, Three Quark Potential in the SU(3) Lattice QCD, *Phys. Rev. Lett.* **86**, 18 (2001).
- [6] T. T. Takahashi, H. Suganuma, Y. Nemoto, and H. Matsufuru, Detailed analysis of the three quark potential in SU(3) lattice QCD, *Phys. Rev. D* **65**, 114509 (2002).
- [7] C. Alexandrou, Ph. de Forcrand, and A. Tsapalis, Static three quark SU(3) and four quark SU(4) potentials, *Phys. Rev. D* **65**, 054503 (2002).
- [8] C. Alexandrou, Ph. de Forcrand, and O. Jahn, The ground state of three quarks, *Nucl. Phys. B, Proc. Suppl.* **119**, 667 (2003).
- [9] S. Kamizawa, Y. Matsubara, H. Shiba, and T. Suzuki, A static baryon in a dual Abelian effective theory of QCD, *Nucl. Phys.* **B389**, 563 (1993).
- [10] Y. Koma, E.-M. Ilgenfritz, T. Suzuki, and H. Toki, Weyl symmetric representation of hadronic flux tubes in the dual Ginzburg-Landau theory, *Phys. Rev. D* **64**, 014015 (2001).
- [11] H. Ichie, V. Bornyakov, T. Streuer, and G. Schierholz, The flux distribution of the three quark system in SU(3), *Nucl. Phys. B, Proc. Suppl.* **119**, 751 (2003).
- [12] V. G. Bornyakov, H. Ichie, Y. Mori, D. Pleiter, M. I. Polikarpov, G. Schierholz, T. Streuer, H. Stüben, and T. Suzuki (DIK), Baryonic flux in quenched and two flavor dynamical QCD, *Phys. Rev. D* **70**, 054506 (2004).
- [13] V. G. Bornyakov, M. N. Chernodub, H. Ichie, Y. Koma, Y. Mori, M. I. Polikarpov, G. Schierholz, H. Stüben, and T. Suzuki, Profiles of the broken string in two flavor QCD below and above the finite temperature transition, *Prog. Theor. Phys.* **112**, 307 (2004).
- [14] F. Bissey, F.-G. Cao, A. R. Kitson, A. I. Signal, D. B. Leinweber, B. G. Lasscock, and A. G. Williams, Gluon flux-tube distribution and linear confinement in baryons, *Phys. Rev. D* **76**, 114512 (2007).
- [15] M. Caselle, G. Delfino, P. Grinza, O. Jahn, and N. Magnoli, Potts correlators and the static three-quark potential, *J. Stat. Mech.* (2006) P03008.
- [16] V. Dmitrašinović, T. Sato, and M. Šuvakov, Smooth cross-over transition from the Delta-string to the Y-string three-quark potential, *Phys. Rev. D* **80**, 054501 (2009).
- [17] O. Andreev, Model of the N -quark potential in $SU(N)$ gauge theory using gauge-string duality, *Phys. Lett. B* **756**, 6 (2016).
- [18] O. Andreev, Some aspects of three-quark potentials, *Phys. Rev. D* **93**, 105014 (2016).
- [19] N. Brambilla, J. Ghiglieri, and A. Vairo, Three-quark static potential in perturbation theory, *Phys. Rev. D* **81**, 054031 (2010).
- [20] N. Brambilla, F. Karbstein, and A. Vairo, Symmetries of the three-heavy-quark system and the color-singlet static energy at next-to-next-to-leading logarithmic order, *Phys. Rev. D* **87**, 074014 (2013).

- [21] O. Kaczmarek, F. Karsch, E. Laermann, and M. Lutgemeier, Heavy quark potentials in quenched QCD at high temperature, *Phys. Rev. D* **62**, 034021 (2000).
- [22] N. Cardoso and P. Bicudo, Lattice QCD computation of the SU(3) string tension critical curve, *Phys. Rev. D* **85**, 077501 (2012).
- [23] M. Lüscher and P. Weisz, Locality and exponential error reduction in numerical lattice gauge theory, *J. High Energy Phys.* **09** (2001) 010.
- [24] M. Lüscher and P. Weisz, Quark confinement and the bosonic string, *J. High Energy Phys.* **07** (2002) 049.
- [25] Y. Koma and M. Koma, The static three-quark potential from the Polyakov loop correlation function, *Proc. Sci., LATTICE2014* (2014) 352.
- [26] Y. Koma and M. Koma, The static potential from the selected intermediate states of gluons, *Proc. Sci., LATTICE2013* (2013) 469.
- [27] O. Jahn and O. Philipsen, Polyakov loop and its relation to static quark potentials and free energies, *Phys. Rev. D* **70**, 074504 (2004).
- [28] M. Koma and Y. Koma, The static three-quark potential of various quark configurations, *Proc. Sci., LATTICE2015* (2016) 324.
- [29] T. T. Takahashi and H. Suganuma, Detailed analysis of the gluonic excitation in the three-quark system in lattice QCD, *Phys. Rev. D* **70**, 074506 (2004).
- [30] M. Albanese, F. Costantini, G. G. Fiorentini, F. Flore, M. Lombardo, and R. Tripiccion (APE Collaboration), Glueball masses and string tension in lattice QCD, *Phys. Lett. B* **192**, 163 (1987).
- [31] Y. Koma, M. Koma, and H. Wittig, Nonperturbative Determination of the QCD Potential at $O(1/m)$, *Phys. Rev. Lett.* **97**, 122003 (2006).
- [32] Y. Koma and M. Koma, Spin-dependent potentials from lattice QCD, *Nucl. Phys.* **B769**, 79 (2007).
- [33] Y. Koma and M. Koma, Scaling study of the relativistic corrections to the static potential, *Proc. Sci., LAT2009* (2009) 122, [arXiv:0911.3204].
- [34] P. Bicudo and M. Cardoso, Iterative method to compute the Fermat points and Fermat distances of multiquarks, *Phys. Lett. B* **674**, 98 (2009).
- [35] C. Ay, J.-M. Richard, and J.H. Rubinstein, Stability of asymmetric tetraquarks in the minimal-path linear potential, *Phys. Lett. B* **674**, 227 (2009).
- [36] S. Necco and R. Sommer, The $N_f = 0$ heavy quark potential from short to intermediate distances, *Nucl. Phys.* **B622**, 328 (2002).
- [37] F. Bissey, A. Signal, and D. Leinweber, Comparison of gluon flux-tube distributions for quark-diquark and quark-antiquark hadrons, *Phys. Rev. D* **80**, 114506 (2009).
- [38] A. S. Bakry, X. Chen, and P.-M. Zhang, Y-stringlike behavior of a static baryon at finite temperature, *Phys. Rev. D* **91**, 114506 (2015).
- [39] A. S. Bakry, D. B. Leinweber, and A. G. Williams, Gluonic profile of the static baryon at finite temperature, *Phys. Rev. D* **91**, 094512 (2015).